Late Holocene tsunami hydrodynamics, sediment provenance and chronology from Dury Voe, Shetland Islands (UK)

Nel NUSSBERGER[1], Max ENGEL[1,2], Tasnim PATEL[3], Alexander VARYCHEV[4], Hans-Peter MEYER[4], Dominik BRILL[5], Anna PINT[6], Philipp KEMPF[2], Katharina HESS[1], Isa SCHÖN[7,8], Vanessa M.A. HEYVAERT[2,9], Sue DAWSON[10]

[1]Heidelberg University, Institute of Geography, Heidelberg, Germany

[2]Institute of Natural Sciences, Geological Survey of Belgium, Brussels, Belgium

[3]Institute of Natural Sciences, MARECO, Marine Ecology and Management, Brussels, Belgium

[4]Heidelberg University, Institute of Earth Sciences, Heidelberg, Germany

[5]University of Cologne, Institute of Geography, Cologne, Germany

[6]University of Hamburg, Institute for Geology, Hamburg, Germany

[7]Institute of Natural Sciences, ATECO, Freshwater Biology, Brussels, Belgium

[8]University of Hasselt, Research Group Zoology, Campus Diepenbeek, Diepenbeek, Belgium

[9]Ghent University, Department of Geology, Ghent, Belgium

[10]University of Dundee, Division of Energy, Environment & Society, Dundee, Scotland

Corresponding author: Nel Nussberger, nussberger@stud.uni-heidelberg.de

ABSTRACT. The Shetland Islands are one of the key sites in the Atlantic Ocean to study tsunami deposits, with three major events identified during the Holocene so far. Here, we aim to (i) reconstruct hydrodynamics of the late Holocene Dury Voe tsunami, (ii) constrain the sediment source area, and (iii) refine its age estimate. Onshore sandy deposits bracketed by thick dystrophic peat as well as marine sediment from the intertidal to offshore zone were sampled at Dury Voe and subjected to laser diffraction grain-size analysis, heavy mineral analysis using energy-dispersive X-ray spectroscopy and foraminiferal analysis. Furthermore, we present the first onshore luminescence dating for deposits on Shetland for quartz and feldspar. The combined results from grain-size and heavy mineral analyses indicate that at least two major tsunami waves entrained fine-grained sediment from the intertidal zone down to ~14 m water depth. The proximal deposit, close to the coast, is separated into a massive and an inversely graded subunit, characteristic of deposition in a very high energy, high-density suspension flow, whilst further inland it shows two fining-upward sequences, characteristic of a suspension grading and lower-energy, lower-density flow. Foraminiferal assemblages are diverse and abundant in the shallow-marine source deposits, but entirely missing in the tsunami deposits onshore, possibly due to post-sedimentary chemical dissolution in the very low-pH environment, which also affected the onshore heavy mineral composition. Data from Bayesian age modelling of the luminescence ages, in combination with pre-existing radiocarbon data, indicate tsunami impact at 470–630 CE. Our findings refine tsunami hydrodynamics at Dury Voe and the overall chronology in the Shetland region, and highlight the role of acidic post-depositional environments in modifying palaeotsunami signatures.

KEYWORDS: Coastal hazards, palaeotsunami, grain-size analysis, sediment provenance, heavy minerals, luminescence dating, foraminiferal analysis

1 Introduction

Tsunamis are a major hazard to coastal communities, infrastructure, and ecosystems and their sedimentary deposits reveal information on occurrence patterns and hydrodynamic conditions beyond instrumental and historical timescales, making them an essential component of coastal hazard assessment (Engel et al., 2020). Palaeotsunami deposits, i.e., deposits of tsunamis "occurring prior to the historical record or for which there are no written observations" (IOC, 2019), expand the available tsunami sedimentary record and help to establish long-term magnitude-frequency patterns for specific regions (Dawson and Shi, 2000; Goff et al., 2012; Weiss and Bourgeois, 2012; Engel et al., 2020; Spiske, 2020).

Since the 1990s, the Shetland Islands have become one of the Atlantic Basin's focal areas of palaeotsunami research (Dawson et al., 2020; Costa et al., 2021). The tsunami deposits on the Shetland Islands occur as layers of fine to medium sand and are preserved in the coastal lakes or bracketed by blanket peat (Bondevik et al., 2005; Dawson et al., 2006; Costa et al., 2021; Engel et al., 2024). These layers typically feature normally graded sands up to 40 cm thick, containing rip-up clasts (from the underlying peat), flame structures, gravel and wood fragments (Bondevik et al., 2003; Costa et al., 2021). Increased concentrations of heavy minerals have been described at the base of some deposits (Costa et al., 2015; Cascalho et al. 2016). All of these features are typical of tsunami deposits worldwide (Dawson and Shi, 2000; Goff et al., 2012; Spiske, 2020).

The most prominent deposit on Shetland results from the Storegga slide tsunami dated to 8175–8120 cal yr BP (Bondevik et al., 2012) and implies an estimated run-up of >30 m at innermost Sullom Voe (Dawson et al., 2020). The layer was documented and sampled in detail at multiple locations on the Shetland Islands with data generated on grain size, diatoms (Bondevik et al., 2005) and heavy minerals (Costa et al., 2015; Cascalho et al., 2016), which represent an important proxy to determine tsunami dynamics and the source of the deposits (Goff et al., 2012; Jagodziński et al., 2012). Two younger, likely tsunamigenic deposits have been identified at different sites, i.e., the Garth (c. 5500 cal yr BP) and Dury Voe (c. 1400 cal yr BP) events (Bondevik et al., 2005; Dawson et al., 2006; Engel et al., 2024). Much less is known about these two younger events; the trigger mechanisms and hydrodynamics are unknown, while data on run-up and sediment provenance remain vague. For the Dury Voe event, run-up has been estimated at c. 9 m above mean sea level (msl) at Basta Voe on Yell (Fig. 1) (Dawson et al., 2006) and up to 3.3 m above msl at Dury Voe (Bondevik et al., 2005).

In this study, we investigate short cores taken from the late Holocene tsunami deposit at Dury Voe, which has first been described and dated to 1500 cal yr BP by Bondevik et al. (2005) at this particular site. The aims of the study are to infer the hydrodynamic conditions and depositional mechanisms during the Dury Voe event and to identify the source area of the palaeotsunami deposits. This will be achieved with high-resolution grain-size analysis as well as energy-dispersive X-ray spectroscopy (EDX) heavy mineral analysis of onshore, intertidal, subtidal and offshore samples. The third aim is to refine the age of the tsunami with the first application of luminescence dating to onshore tsunami deposits on the Shetland Islands and Bayesian age modelling of all available chronostratigraphic data.

2 The Shetland Islands and study site

The Shetland Islands (Figure 1) comprise >100 individual islands located between the North Atlantic Ocean, the Norwegian Sea and the North Sea. The islands are underlain by the Orkney-Shetland Platform, which separates the North Sea from the northeast Atlantic and is part of the Caledonian Orogenic belt consisting of several terranes that were joined in the Late Silurian. Three major parallel fault lines run through the archipelago in a north–south direction, resulting in a complex pattern of metamorphic and metasedimentary as well as igneous provinces (Figure S1) (Gillen, 2003; Hall et al., 2021).

The topography is strongly controlled by the repeated cycles of Pleistocene glaciation and deglaciation (Ross et al., 1993; Bradwell et al., 2021). During the most recent glaciation period, c. 30,000–15,000 years ago, Shetland was covered by an independent ice cap (Bradwell et al., 2021; Hall et al. 2021; Clark et al., 2022). Glacial landforms are located mostly offshore but glacial till is also found underneath the Holocene blanket peat and exposed at many locations (Figure S1A). Lateglacial to Holocene sea-level rise led to the formation of fjords, locally referred to as “voes”, with calmer waters than the exposed high-energy cliff coasts (Firth and Smith, 1993; Smith, 1993). The onshore topography is generally low, characterised by low hills and ridges with shallow valleys infilled with Holocene sediments (Hall et al., 2021). Holocene relative sea-level change is to date poorly constrained, with estimates of c. 34–17 m below present msl at the time of the Storegga event and c. 1 m below present msl at the time of the Dury Voe event (Bondevik et al., 2005; Dawson et al., 2020).

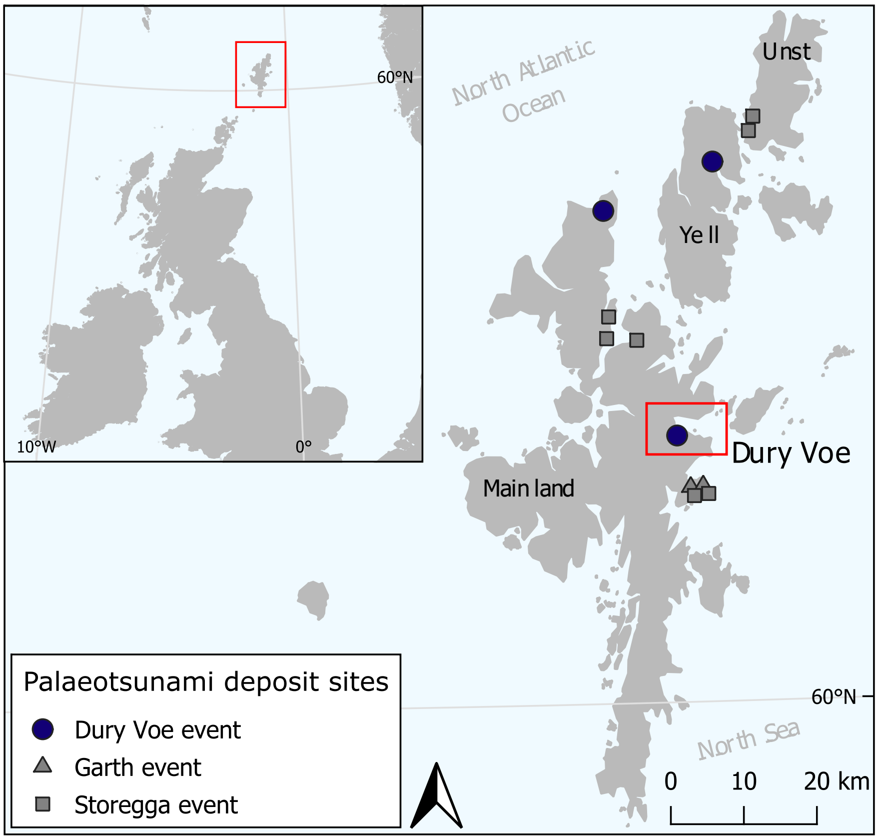

Figure 1. *Map of the Shetland Islands with the study site of Dury Voe marked with rectangles (refer also to Figure 2A). Markers represent deposit sites described on the Shetland Islands (based on Bondevik et al. 2005, Engel et al. 2024). Inset shows position of the Shetland Islands north of Scotland, between the North Atlantic Ocean, Norwegian Sea, and North Sea (basemap: EuroGeographics, 2023).*

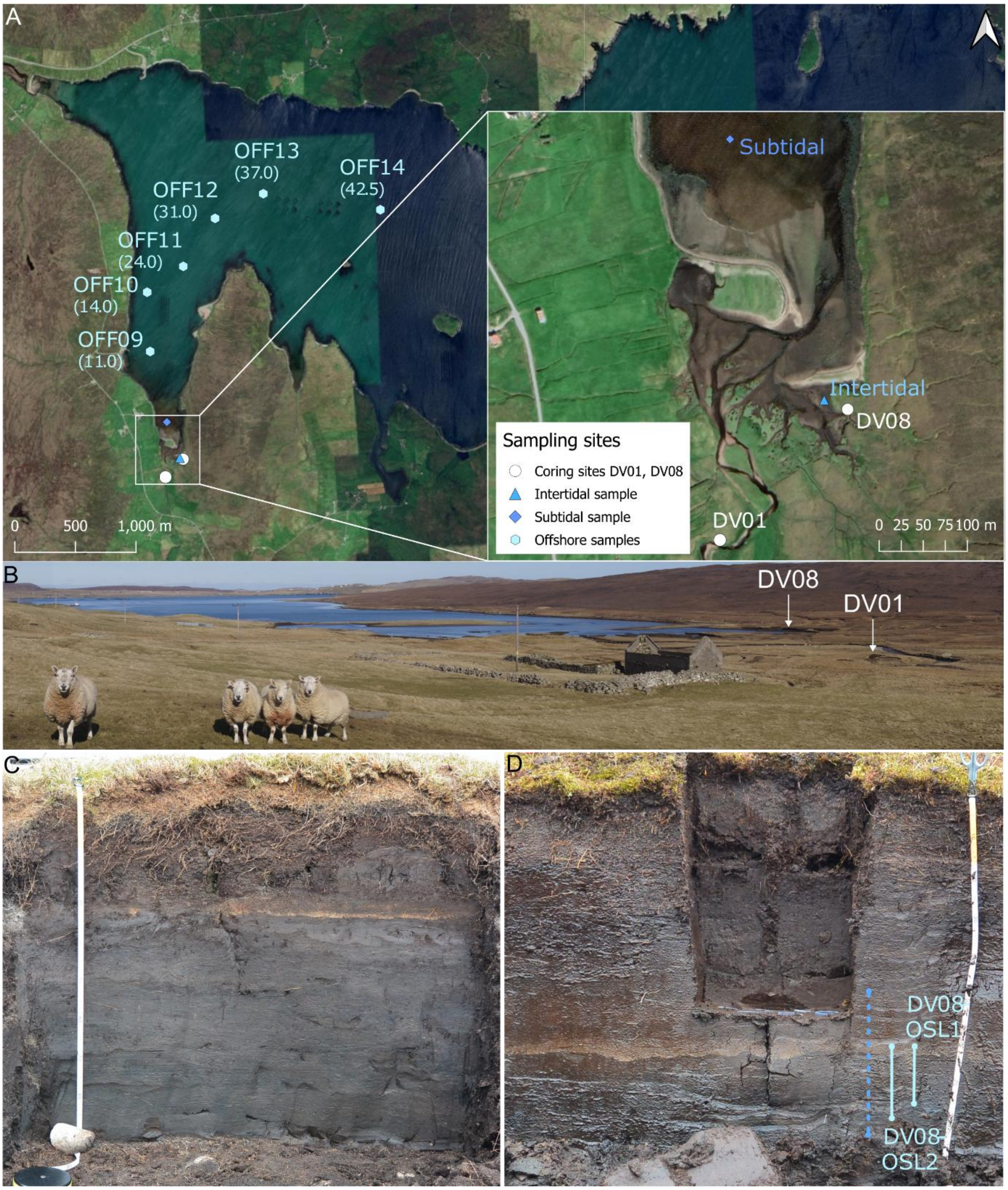

Figure 2. *A) Satellite image of the sampling sites at Dury Voe. Circles represent coring sites DV01 and DV08, hexagons represent offshore samples, the diamond represents the subtidal sample, the triangle represents the intertidal sample. Water depths for offshore sampling sites are given in metres bsl (below sea level) in brackets. Basemap: Google ©2024, Airbus, Maxar Technologies, integrated into QGIS via XYZ Tiles. B) Panoramic view of the Dury Voe site taken from the SW margin of the inset of Figure 2A. C) Profile at DV01. D) Profile at DV08. Sample position for environmental dose rate estimation is shown as a dashed line, the sample positions for luminescence dating as solid lines.*

Dury Voe is located on the east coast of Mainland. Its water depth descends from the innermost shore down to c. 50 m where it opens towards the North Sea (Figures 1, 2A). The local topography is characterised by low hills and blanket peat covering gravelly glacial deposits (Figures 2B, S2A). A small creek cuts the blanket peat and exposes vertical sections (Figure 2C, D). The deposit presents as a light brown sand layer ranging between 5 to <1 cm thickness, and reaches c. 400 m inland, (Bondevik et al., 2005). In the intertidal zone, sand and gravel bars form by a moderate longshore current interplaying with the debouching creek. A series of sampling sites were located on a transect running NO-SW. Sampling site DV01 is located c. 200 m inland from the innermost part of Dury Voe, where the deposit already becomes discontinuous. The second site of DV08 is located c. 25 m from the shore (Figure 2A). Six offshore (OFF) samples were collected inside Dury Voe covering water depths from the intertidal to 42.5 m (Figure 2A, Table S1).

3 Materials and Methods

3.1 Fieldwork and sampling

At Dury Voe, short push cores were taken at eight sites; the sites DV01 and DV08 were analysed in detail to represent a site close to the shore as well as one located further inland where depositional patterns are expected to change. Offshore samples (OFF09–OFF14) were taken using an Ekman-Birge grab sampler from a fishing boat with an automatic winch. Intertidal and subtidal samples representing the modern sedimentary environment were taken by hand and with a push core from the seafloor surface, respectively.

The cores were cut in half lengthwise, described, photographed, sealed and stored at the laboratories of the Geological Survey of Belgium, Institute of Natural Sciences, Brussels. All subsequent preparatory steps as well as grain-size analysis were carried out at the Laboratory of Geomorphology and Geoecology, Institute of Geography, Heidelberg University. EDX analysis was carried out at the Ion Probe Laboratory and the Laboratory for Raster Electron Microscopy, Cathodoluminescence and micro-Raman, Institute of Geosciences, Heidelberg University.

Samples for grain size analysis were taken with a spatula from the sandy layers within core DV01 and DV08 in increments of 2 mm, resulting in 25 samples retrieved from core DV01 and 20 samples from core DV08. Due to low amounts of clastic grains and high organic content, samples DV01_23–DV01_25 and DV08_20 were excluded from measurement, resulting in 22 samples analysed from DV01 and 19 samples from DV08. The remaining sand material of both cores were sampled in 5 mm increments and used for heavy mineral analysis, resulting in 10 samples from core DV01 and 8 samples from DV08. Due to low heavy mineral yield at the top of the cores, samples DV01/07-08 and DV01/09-10 were combined prior to EDX, resulting in a total of 8 samples for DV01. In the same manner, DV08/07-08 was combined resulting in a total of 7 samples for DV08.

3.2 Geophysical measurements

A Geotek multi-sensor core logger at the Renard Centre of Marine Geology, Ghent University, Belgium, was used to obtain high-resolution photographs taken by the Geoscan IV Linescan imaging system. Bulk density (γ-ray attenuation densometer) and the CIELAB colour space (Konica Minolta CM-700d spectrophotometer) were measured in increments of 2 mm.

3.3 Grain size analysis and pH value measurements

The grain size distribution of the offshore samples and the sand sections in DV01 and DV08 was measured by laser diffraction (Fritsch Analysette 22 NeXT Nano). For the offshore samples, the coarse skeletal fragments were removed using a 2 mm sieve. All samples were pre-treated with H_2O_2 (15 %) to remove organic matter and 0.1 M $Na_4P_2O_7$ for aggregate dispersion, before automated agitation overnight and triplicate measurement. Univariate statistical parameters after Folk and Ward (1957) were derived from GRADISTAT v9.1 (Blott and Pye, 2001); R v4.5.0 and RStudio v2024.12.1 in combination with R packages ggplot2 v3.5.2, ggpubr v0.6.0, readxl v1.4.5, tidyverse v2.0.0., viridis v0.6.5, and writexl v1.5.4 were used for all data visualisation. The vertically confining peat from both cores was cut into aliquots of c. 10 g, which were dissolved in 1 M KCl and measured for their pH value using a WTW PH 320 pH meter.

3.4 Heavy mineral analysis by energy-dispersive X-ray spectroscopy

Dried offshore and intertidal samples were carefully crushed with a mortar and pestle and wet-sieved at 200 µm and 63 µm to retain the fine sand fraction. The fine sand was treated with HCl (25 %) and heated to 80 °C for 20 min to eliminate oxide coatings and carbonates. Samples were then washed and tested with $AgNO_3$ to ensure the removal of chloride. Heavy liquid separation of each individual sample was carried out using 30–45 ml sodium polytungstate (SPT, $3\ Na_2WO_4 \cdot 9\ WO_3 \cdot H_2O$) at a density of 2.86 g/cm³ in 50 ml separatory funnels following the protocol outlined in Boenigk (1983). The heavy mineral fraction at the bottom of the funnel was isolated using a fitted vacuum pump with a cellulose acetate filter paper. Samples from DV01 and DV08 were treated the same way, except for additional removal of organic matter through H_2O_2 (30 %) before wet-sieving and treatment with diluted HCl (12.5 %) due to a very low carbonate content. For the EDX analysis, the samples were placed in plexiglass moulds, dried at 70 °C, cast in CaldoFix-2 epoxy resin (Struers), and centrifuged to minimise air inclusions. The resin-cast samples were sanded on silicon carbide paper and finally polished with 1 µm and 0.25 µm polycrystalline diamond polishing paste. Samples were analysed using a ZEISS EVO MA 15 scanning electron microscope (Carl Zeiss Microscopy) with an X-Max 150 mm² silicon drift detector (Oxford Instruments) and AZtec Nanoanalysis Software v6.0 SP1. Accelerating voltage was 18 kV, specimen current 400 pA. To facilitate the visualisation of mineral composition, identified minerals were grouped in Table S2.

3.5 Multivariate statistical analysis

End-member modelling analysis (EMMA) was performed on the grain size distribution (GSD) using the R package EMMAgeo v0.9.8. EMMA is an algorithm originally developed for statistical unmixing sediments from multiple sources by identifying underlying distributions (loadings) and their relative contribution (scores). Loadings are a direct proxy of the processes that cause the characteristic GSD while scores represent the influence of the respective process on the sediment deposit (Dietze and Dietze, 2019).

EDX data were analysed by principal component analysis (PCA) and hierarchical clustering (HC) using the R package ggbiplot v0.55 and cluster v2.1.8.1, respectively, to explore and visualise patterns of variance and similarity among the samples (Jolliffe and Cadima, 2016). Due to imperfect heavy liquid separation, some samples contained particles other than heavy minerals, e.g., quartz and feldspars. These particles were excluded from statistical analysis. The PCA was performed on log-transformed EDX data. HC groups similar elements by minimising intra-cluster variances in a hierarchical manner (Nielsen, 2016) and is visualised as a dendrogram. Clusters were defined using Euclidean distance and Ward's linkage method, and the optimal number of clusters was determined through internal validation with the R package clValid v0.7 and robustness tested with pvclust v2.2-0.

3.6 Foraminiferal analysis

All modern offshore and intertidal samples from Shetland and selected ones from the tsunami sands of DV01 were investigated for foraminiferal content. Samples of c. 10 cm³ were wet-sieved through 63 µm and 100 µm and picked under a binocular microscope up to a maximum of 300 specimens. All foraminiferal taxa of these samples were determined at least to genus level, using the databases of WoRMS (WoRMS Editorial Board, 2025) and Foraminifera.eu (Hesemann, 2015) as well as regional literature, especially Horton and Edwards (2006). Taxonomic determination was supported by scanning electron microscope (SEM) imaging, carried out at the Institute of Natural Sciences, Brussels (Figure S6).

3.7 Luminescence dating

Luminescence dating was applied to two individual samples from the sand layer in DV08 to independently test existing radiocarbon dates from the site (Bondevik et al., 2005) and to overcome associated uncertainties. In contrast to sandwich dating by radiocarbon, luminescence directly dates the time of deposition and is not affected by the hiatus resulting from the basal erosional contact (Brill and Tamura, 2020). Samples were collected in light-proof PVC tubes and analysed at the Cologne Luminescence Laboratory under dimmed red-light conditions. Sample preparation of coarse grain (150–200 µm) quartz and feldspar extracts included dry-sieving, treatment with HCl (10 %) to remove carbonates, with H_2O_2 (10 %) to remove organic matter and with sodium oxalate (10 %) to destroy clay aggregates. Density separation with sodium polytungstate ($3\ Na_2WO_4 \cdot 9\ WO_3 \cdot H_2O$) was used to extract potassium-rich feldspar (<2.58 g/cm³) and quartz (>2.62 g/cm³ and <2.68 g/cm³). Quartz samples received a final etch with HF (40 %) for 40 min followed by an HCl wash to remove any feldspar contamination and the alpha-radiation affected outer rim of the grains.

Dose rates are based on radionuclide contents derived with high-resolution gamma spectrometry using an Ortec PROFILE M-Series GEM Coaxial P-type gamma spectrometer and the conversion factors of Guérin et al. (2011). Due to the small thickness of the sand layer, gamma dose rates had to be reconstructed using the layer model of Riedesel et al. (2019). Water content was determined by measuring water loss after drying the samples at 50 °C. Internal dose rates for feldspar extracts were based on empirical potassium contents of 10±2 % (Smedley et al., 2012). The alpha radiation contribution in feldspar was calculated with an a-value of 0.11±0.02 (Kreutzer et al., 2014). Cosmic dose rates were estimated based on geographic location, depth below surface and a sediment density of 1.8±0.1 g/cm³ following Prescott and Hutton (1994). Calculation of total dose rates was based on the online calculator DRAC (Durcan et al., 2015).

For burial dose determination, quartz and feldspar extracts were fixed on steel discs using silicon spray to create aliquots with 8 mm and 2 mm (quartz) or 1 mm (feldspar) diameter. Feldspar grains were also measured on single grain discs with 300 µm hole diameter. All discs were measured on a Risø TL/OSL DA-20 reader equipped with a $^{90}Sr/^{90}Y$ beta source delivering ~0.1 Gy/s at the sample position. Luminescence signals were stimulated with blue LEDs at 125 °C (quartz) and infrared LEDs (multigrain) or an infrared laser (single grain) at 50 and 150 °C (feldspar). Luminescence emissions were filtered with a 7.5 mm Hoya U340 (quartz) or a 410 nm interference filter (feldspar). All quartz measurements followed a SAR protocol (Murray and Wintle, 2000) with preheat at 220 °C for 10 s and cut-heat at 200 °C. Feldspar samples were measured with a post-infrared-infrared protocol ($pIRIR_{150}$; Brill et al., 2018) with two successive IR stimulations at 50 °C (IR_{50} signal) and 150 °C ($pIRIR_{150}$ signal).

The appropriateness of the quartz protocol was tested with a preheat-plateau test that indicates equivalent doses independent of preheat temperatures between 180 °C and 280 °C. In addition to that, dose-recovery tests at 220 °C demonstrate adequate reproducibility of laboratory doses in the range of the natural dose for both samples (mean dose-recovery ratios of 0.97–0.98). The $pIRIR_{150}$ protocol was evaluated using dose-recovery tests and residual dose measurements after signal resetting in a Dr. Hönle Sol2 solar simulator for 24 h. Dose-recovery ratios range between 0.99 and 1.10, laboratory residual doses remain below 0.5 Gy for both samples and signals.

Equivalent doses were determined for 17–36 multigrain aliquots and 92–242 single feldspar grains per sample. For all samples with normally distributed dose values, burial doses were calculated using the central age model (CAM; Galbraith et al., 1999), whereas the minimum age model (MAM; Galbraith et al., 1999) was applied to right-skewed dose distributions. All feldspar ages were corrected for fading using the approach of Huntley and Lamothe (2001) and signal and sample-specific g-values of 0.8±0.2 to 5.0±0.3 % per decade.

3.8 Bayesian age modelling

The Bayesian age model ‘coffee’ (R package coffee, v.0.4.3; Blaauw et al., 2024) was used to integrate available radiocarbon data on the late Holocene tsunami from literature and luminescence ages of the present study to narrow down the timing of the event. ‘Coffee’ represents a Bayesian modelling approach for chronological ordering and increases the precision of ages of stratigraphies or individual stratigraphic layers for which a number of age datings are available (Blaauw et al., 2024). We used four radiocarbon ages from Bondevik et al. (2005) with their 2σ error range: two located above the upper boundary of the sandy event layer (*terminus ante quem*) and two below the lower boundary of the sandy event layer (*termini post quem*) from both Dury Voe and Basta Voe (Table S3). Dates situated more than 5 cm above or below the event deposit were excluded (e.g., TUa-3489, cf. Bondevik et al., 2005). The luminescence dates from this study as well as the modelled age from Loch Flugarth (Engel et al., 2024) as derived from the Bayesian age-depth model of Hess et al. (2023, 2024) represent *termini ad quem* (Table S4). All radiocarbon ages were calibrated within the coffee-model using the IntCal20 calibration curve (Reimer et al., 2020). The model was run using the 2σ error range and 700,000 Markov chain Monte Carlo (MCMC) iterations. In total, 85.37 % of the modelled ages fell within the 95 % highest posterior density ranges of the unmodelled dates, indicating good agreement between modelled and observed ages.

4 Results

4.1 Sand layer description and geophysical parameters

Both cores comprise a light brown layer of medium to fine sand of c. 5 cm (DV01, Figures 3, S2) and 4 cm (DV08, Figures 4, S3) thickness, respectively, vertically confined by dark brown dystrophic peat with pH values of 3.0–3.4 (Figure S4). Around DV01, this layer becomes discontinuous (Figure 2C). The lower boundaries are sharp and appear erosional, the upper boundaries are less distinct. Towards the top, the sand layers become increasingly darker (brightness value L*), while the density decreases (Figures 3, 4). Roots reach from the top peat layer into the sand and are visible throughout the cores.

4.2 Grain-size analysis

DV08 is comprised of medium sand, fine sand and coarse silty fine sand. Samples show predominantly leptokurtic, very fine-skewed unimodal distributions with a maximum in the fine to medium sand class (Figures 3, 5B). Sorting is moderate to poor. Mean grain sizes range from 153–256 µm. Both the heatmap and GSDs show a clear shift towards coarser grain sizes in the upper 1.8 cm of the core, corresponding to samples DV08_12–19. In this upper unit, the mean grain size first coarsens upwards from 211–256 µm, then fluctuates between 239–246 µm. The lower subunit shows no clear trend and appears massive.

DV01 is comprised of fine sands and coarse silty sands with leptokurtic to very leptokurtic, fine- to very fine-skewed unimodal distributions with a maximum in the fine-sand class (Figures 4, 5A). Mean grain sizes range from 171–199 µm. Sorting is moderate to poor. DV01 has finer grain sizes overall, with no sample being classified as coarser than fine sand. A shift in grain size is not as clearly visible as in DV08, but a lower fining upward subunit can be differentiated from an upper, massive to slightly fining upward subunit, with the boundary at c. 2.6 cm from the top of the sand layer.

The EMMA of GSDs determined three end-members to explain the variance between the sand samples of core DV08. EM1 shows a global maximum at 190 µm (fine sand), a local maximum at 400 µm (medium sand) and a small silt component. EM2 has a similar distribution, but with a smaller coarse silt component. EM3 has a major peak at 400 µm and a very small one around 190 µm, representing the coarsest distribution of all three EMs (Figure 5C).

The bottom part of DV08 (samples 01–05) is represented by EM1 to a very high degree, with EM2 and, successively, EM3 showing relative contributions of <10 %. Samples 06 to 11 show an increasing influence of EM2 replacing the one of EM1 (only 10 % in sample 10). Samples 12–18 show a dominance of EM3, correlating with the coarsening-up trend inferred from the mean grain size values. The samples that show the peak shift in the GSDs are mostly determined by EM2 and EM3 (Figure 5C).

The offshore samples show very poor sorting, comprising a strong fine-sand component and silts, medium to fine and coarse sands and up to cm-size skeletal fragments, the latter especially present at water depths ≥24 m (Figure 6).

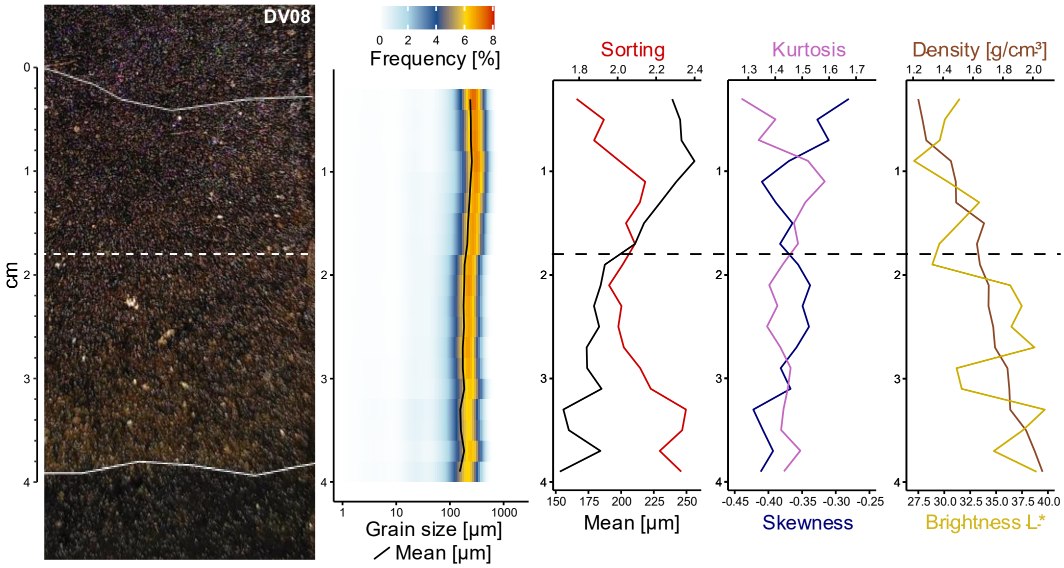

Figure 3. *Photograph of split core DV08 from Dury Voe site, with heat map of grain-size distribution, mean, sorting, kurtosis, density and brightness (L*). The subunit boundary is marked by the dashed line.*

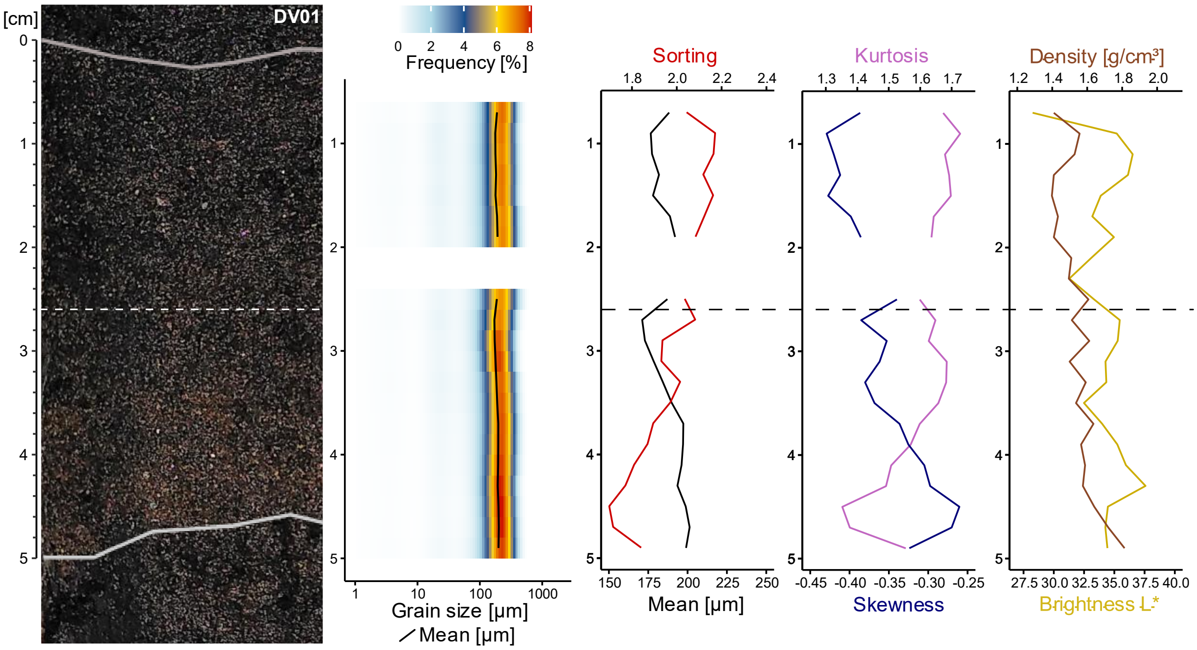

Figure 4. *Photograph of core DV01 (refers to section 6-14 cm in Figure S2) from Dury Vie site, with heat map of grain-size distribution, mean, sorting, kurtosis, skewness, brightness (L*) and density. Samples DV01_14 and DV01_15 had to be excluded from statistical analysis due to low confidence in the measured values. The subunit boundary is marked by the dashed line.*

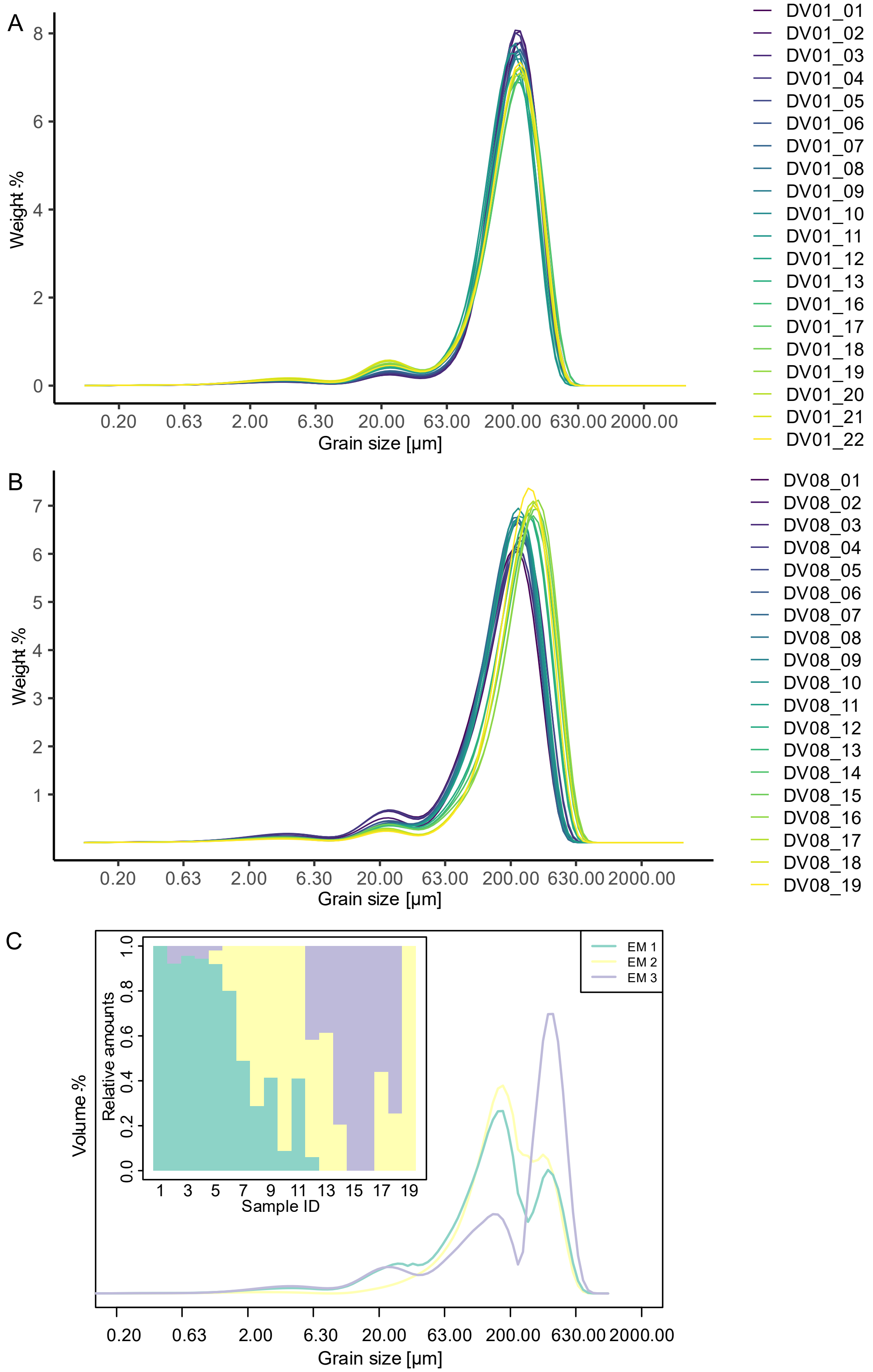

Figure 5. *A) Grain-size distributions of the core from Dury Voe site DV01. Samples DV01_14 and DV01_15 were excluded due to low statistical reliability of the measurement. B) Grain-size distributions of the core from Dury Voe site DV08. C) Grain size distributions of end-members (EM) 1–3 as well as relative amounts of EMs explaining the distributions of samples of DV08.*

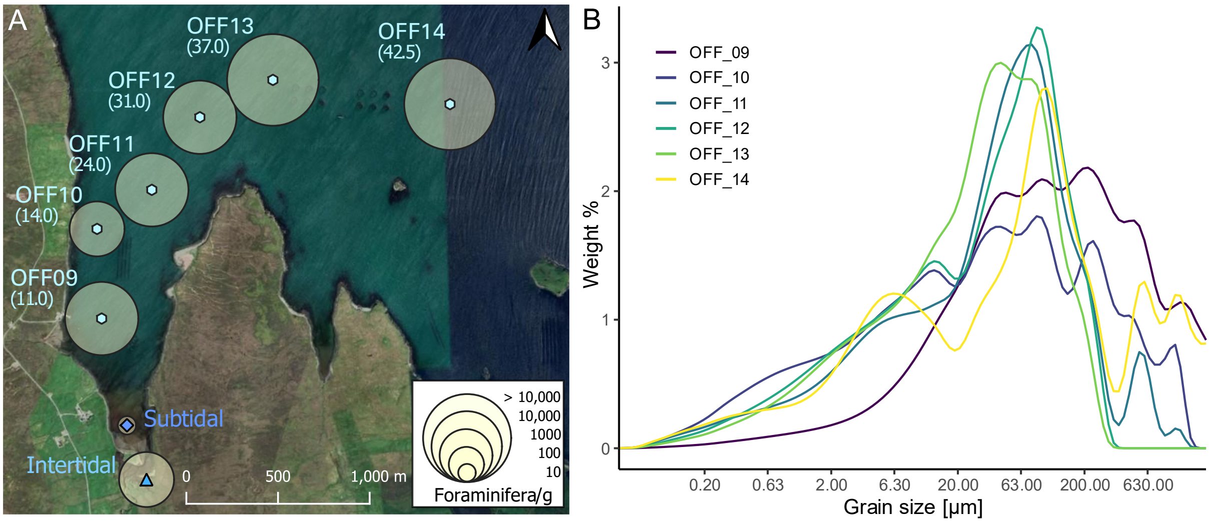

Figure 6. *A) Modern intertidal and offshore sampling sites at Dury Voe (Figure 2A), with depths in metres bsl (below sea level) given in brackets, foraminiferal concentrations and B) grain size distributions. Basemap: Google ©2024, Airbus, Maxar Technologies, integrated into QGIS via XYZ Tiles.*

4.3 Heavy-mineral analysis

The heavy-mineral content in core DV01 ranges from 0.37–0.93 %, with the highest content in the uppermost combined sample (Figure 7). The lower fining-up sequence contains 0.37–0.39 % heavy minerals in the bottom samples and around 0.50 % at the top, signifying a slight increase towards the top. This is in accordance with the measured density values (Figure 3). The upper sequence shows similar heavy mineral contents with a slightly elevated content, except for sample DV01/07-08 (0.24 %). Core DV08 closer to the shore has a higher heavy mineral content of 0.28–2.96 %, with the highest concentration in the uppermost combined sample as well as the lowest part of the core, where the measured density peaks (Figure 4). The massive lower unit shows a decrease in concentration towards the top except for the second sample. The inversely graded upper unit shows a distinct, continuous increase in heavy minerals towards the top.

DV01 is dominated by epidote (60.09–71.22 %) and amphibole (10.20–23.52 %). Within the amphibole group, hornblende is by far the most abundant mineral. Other abundant minerals include tourmaline and minerals of the haematite group. Tourmaline with a <15 % and mica and haematite group minerals with <10 % are common but their content between samples varies strongly. Epidote and amphibole concentrations vary across the core but show no clear trends. The top 1 cm of the upper unit contains more tourmaline than amphibole. The only observed mica group mineral is muscovite, which is more abundant towards the upper parts of the subunits. Zircon shows no clear trend in the lower unit but a distinct decrease towards the top in the upper unit. Tourmaline is abundant throughout the core with relatively high contents in the upper unit (7.10–13.30 %). The lower unit shows a slight increase in tourmaline towards the top.

DV08 samples contain mostly epidote (36.32–58.26 %) and amphibole (27.83–57.71 %), i.e., a higher amphibole/epidote ratio than DV01. The abundance of specific minerals within the groups is very similar to DV01, with the amphiboles mainly consisting of hornblende, some tremolite and unspecified amphibole, and the epidote group mainly comprising epidote and zoisite. Other common heavy minerals with fractions <10 % are tourmaline, haematite, and mica but their content between samples varies strongly. Amphibole concentrations increase slightly towards the top of both subunits while epidote concentrations slightly decrease. A sharp increase in epidote and decrease in amphibole coincide with the subunit boundary at c. 1.8 cm depth. The only mica present is muscovite; DV08 has a higher muscovite content than DV01. It is most abundant in the upper subunit, with a slight increase towards the top. Tourmaline is most abundant at the top of the upper subunit (9.09 %) and moderately frequent across the rest of deposit (0–3.48 %). DV08 has less tourmaline than DV01 overall. Zircon is largely absent in the lower, massive unit, but reaches percentages of 1.81–3.33 % at the top of the upper unit.

The intertidal sample is dominated by epidote (50.70 %) and amphibole (30.41 %) and contains >5 % spinel group minerals. Tourmaline, mica group minerals and pyroxene contribute >3 %, all other minerals contribute around 1 % or less to the composition of the sample.

The subtidal sample contains mainly epidote (55.57 %) and amphibole (24.09 %). Spinel group minerals are absent. Tourmaline and pyroxene contribute >2 %, all other minerals contribute around 1 % or less to the composition of the sample.

Offshore samples are generally more diverse than onshore samples. They are also dominated by amphibole (31.25–59.48 %), mainly hornblende, unspecified amphibole, and few tremolite and actinolite, as well as epidote (12.27–40.74 %), mainly epidote and zoisite in similar percentages. All offshore samples contain more pyroxene and diopside than DV01 and DV08. Other frequent heavy minerals across all offshore samples are pyroxene, especially in OFF12 and OFF13 (both >10 %), and diopside, especially in OFF12 and OFF13 (both >10 %). Spinel is especially abundant in OFF10 (7.00 %) but infrequent or absent in other offshore samples. Garnets are more frequent offshore than onshore and contribute between 1.74–9.87 % to offshore samples, except for OFF09 (0.36 %).

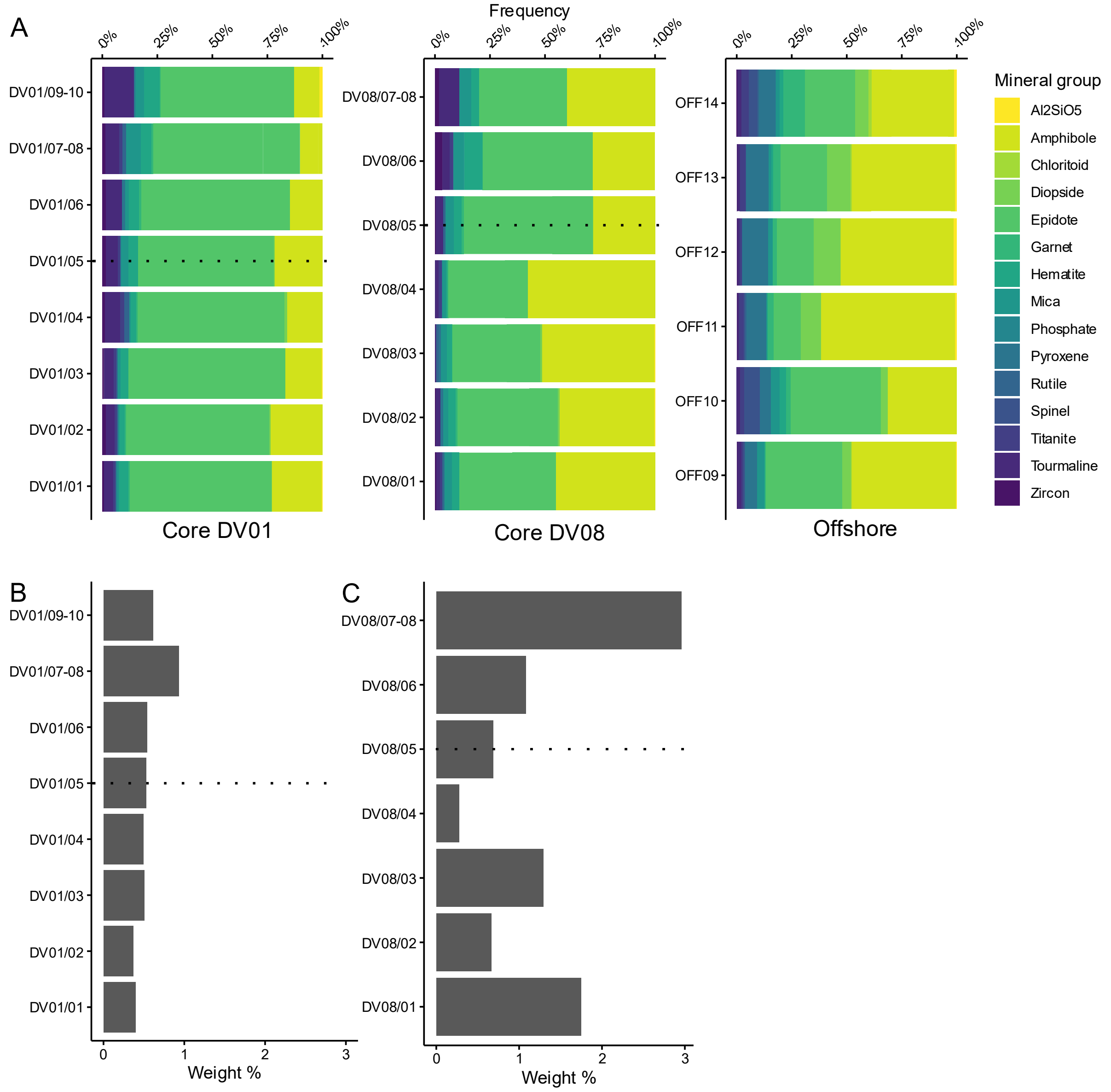

Figure 7. *A) Heavy mineral composition of tsunami deposit cores DV08, DV01, and offshore (OFF) samples from Dury Voe site, separated into heavy mineral groups. B) Total heavy mineral content of DV01 samples. Especially samples DV08/05, DV08/06 and DV08/07-08 contained considerable quartz and feldspar impurities, affecting the apparent heavy mineral content (see Table S8). C) Total heavy mineral content of DV08 samples. Dashed lines mark subunit boundaries. Samples DV01/09-10 contained quartz and feldspar impurities, affecting the apparent heavy mineral content (see Table S8).*

In the PCA, the first two components explain 39.7 % (PC1) and 14.9 % (PC2) of the variation of the dataset, respectively. Samples of the onshore tsunami deposit cluster very closely due to their similar compositions, whereas offshore samples with their more diverse composition are less tightly clustered. The subtidal and intertidal samples are closely related to the onshore clusters, especially DV08. The arrangement of clusters reflects the geographical arrangement of the sample sites, with the intertidal and subtidal samples showing similarity to the proximal to shore onshore (DV08) and offshore (OFF09, OFF10) samples and dissimilarity to the distal onshore (DV01) and offshore samples (OFF11–14). From the offshore samples, OFF10 (14 m bsl) has the closest mineral composition to the subtidal and onshore samples. OFF09 (11 m bsl) is also similar in composition. The deeper and further offshore samples OFF11–14 are less similar. The arrows reflect how the original variables relate to the PCs and indicate that the cluster of onshore samples is strongly influenced by diopside, pyroxene and amphibole content, while offshore samples are more influenced by epidote, haematite, zircon, chloritoid and tourmaline content. HC of the samples reflects the results from PCA, showing that OFF09 and OFF10 cluster closely with the onshore samples as well as the intertidal and subtidal samples.

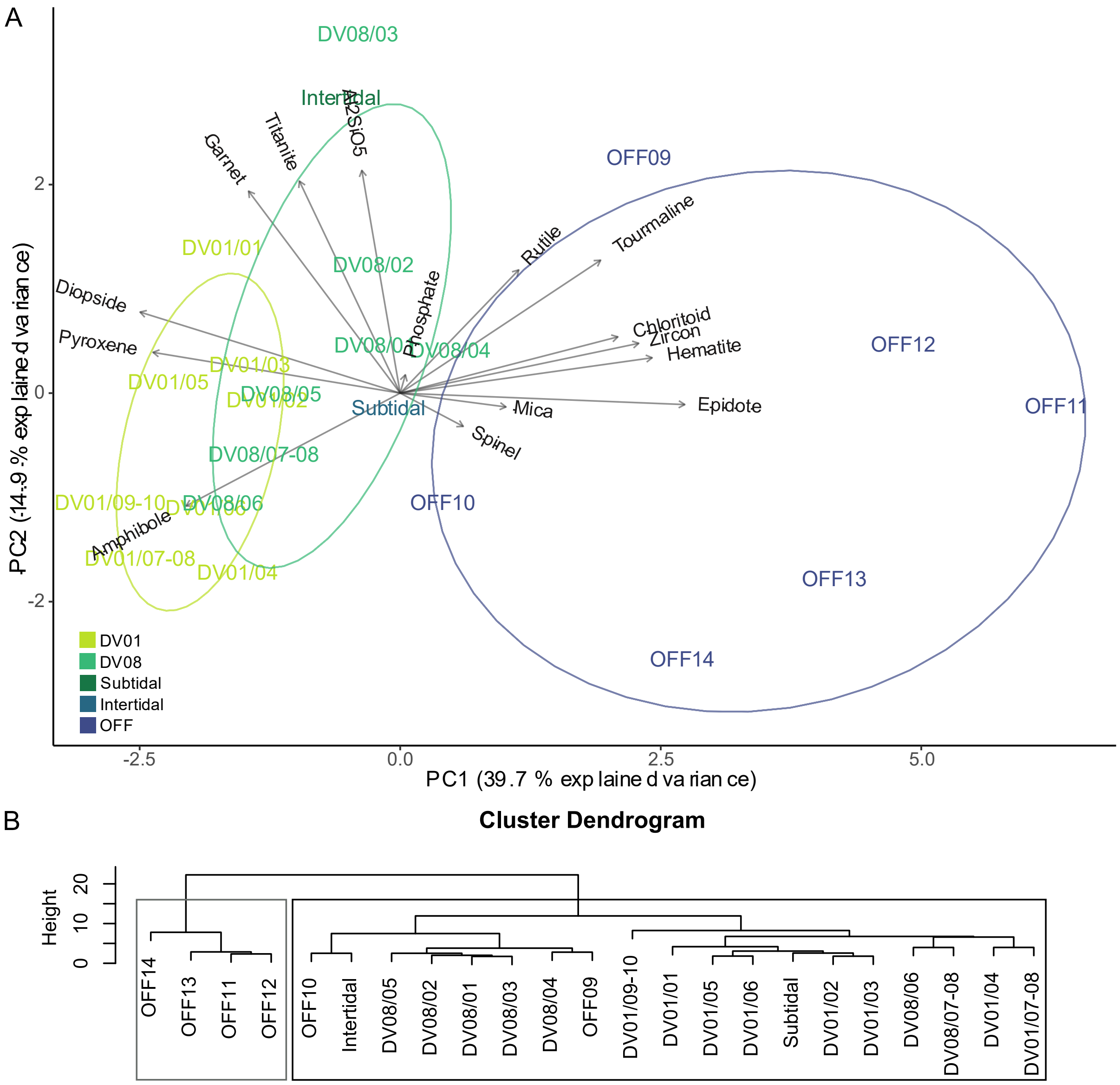

Figure 8. *A) Biplot of Principal component analysis (PCA) results. Samples from the same location or sampling group are indicated by the same colour. Arrows indicate how original variables relate to Principal components (PCs). B) Cluster dendrogram from hierarchical clustering (HC) using Euclidean distance and Ward's linkage (see Table S10 for statistical tests).*

4.4 Foraminiferal study

Foraminiferal concentrations in modern sediments from within Dury Voe range from low/moderate (intertidal) to high (deeper subtidal) (Figure 6A). The diversity ranges from two taxa in the intertidal (*Miliammina fusca, Elphidium williamsoni*) to almost 60 in the four deepest samples (dominated by *Cibicides lobatulus, Egerella scabra*) (Figures S6, S7).

However, all samples investigated from the onshore sand layers in DV01 and DV08 were completely void of foraminifera as well as of any skeletal grain or other carbonate component.

4.5 Luminescence dating

Quartz from the study area shows stable and fast-component dominated luminescence signals. However, the intensities of the signals are insufficient for analysing 1 mm aliquots or smaller. Feldspars show much higher signal intensities that allow for measuring even single grains. All signals and aliquot sizes are characterized by low to moderate dose scatter (10–40 % over-dispersion) and normally distributed to slightly right-skewed equivalent dose distributions. Overall, final ages show good agreement among different signals and aliquot sizes for individual samples, and between the ages of both samples (Figure 9, Table 1). All six ages combined yield mean values of 1360±50 years for DV08-1 and 1460±80 years for DV08-2. There are only a few outliers at the lower end (1100 years: IR_{50} single-grain age for DV08-2, 1200 years: $pIRIR_{150}$ single-grain age for DV08-1) and the upper end (1700 years: $pIRIR_{150}$ small aliquot age for DV08-2).

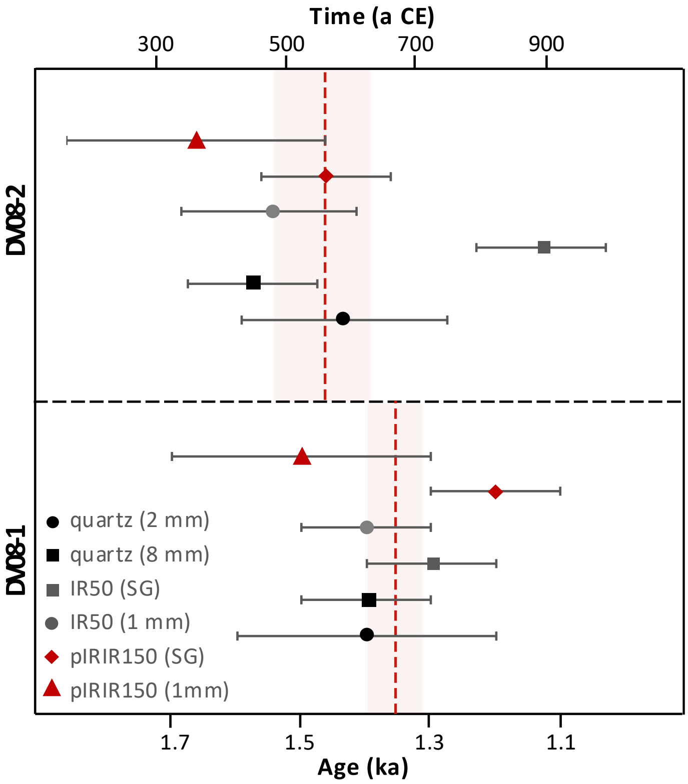

Figure 9. *Luminescence ages of the two samples from the tsunami deposit DV08 at Dury Voe site, using different minerals, signals and aliquot sizes.*

Table 1*. Luminescence ages of tsunami deposit of DV08 at Dury Voe site (SG = single grains, N = number of accepted aliquots/grains, OD = over-dispersion, AM = age model, Age unc. = uncorrected age, Age cor. = age corrected for fading; bold, shaded numbers indicate ages used for the age depth model).*

Sample	Lab-ID	Signal	Size	N	OD (%)	AM	Burial dose (Gy)	Age unc. (ka)	g-value (%/decade)	Age cor. (ka)
DV08-1	C-L5183	Quartz	2 mm	31	26±4	MAM	2.5±0.3	**1.4±0.2**	-	-
			8 mm	23	9±2	CAM	2.4±0.1	**1.4±0.1**		
		IR50	SG	141	34±2	CAM	2.1±0.1	0.9±0.1	4.2±0.1	**1.3±0.1**
			1 mm	22	14±2	CAM	2.3±0.1	1.0±0.1		**1.4±0.1**
		pIRIR150	SG	92	28±3	MAM	2.7±0.2	1.1±0.1	0.8±0.2	**1.2±0.1**
			1 mm	17	18±4	MAM	3.4±0.3	1.4±0.2		**1.5±0.2**
DV08-2	C-L5184	Quartz	2 mm	26	23±4	MAM	2.5±0.2	**1.4±0.2**	-	-
			8 mm	21	11±2	CAM	2.7±0.1	**1.6±0.1**		
		IR50	SG	242	44±2	CAM	1.8±0.1	0.8±0.1	5.0±0.3	**1.1±0.1**
			1 mm	36	29±4	CAM	2.4±0.1	1.0±0.1		**1.5±0.2**
		pIRIR150	SG	138	36±3	MAM	2.9±0.1	1.2±0.1	2.4±0.1	**1.5±0.1**
			1 mm	32	34±5	MAM	3.3±0.3	1.4±0.2		**1.7±0.2**

5 Discussion

5.1 Depositional process

The deposit at Dury Voe is interpreted as tsunamigenic based on its presence as a thin layer of light-brown fine to medium sand between thick layers of dark brown dystrophic blanket peat, becoming discontinuous at least from 200 m inland. The layer can be traced inland for c. 400 m and to 3.3 m above high tide along the valley floor (Bondevik et al., 2005). In DV08, the layer has a thickness of 4 cm, at DV01 further inland the thickness is 5 cm. The increased thickness at site DV01 is most likely caused by the microtopography, as a general landward thinning trend was identified by Bondevik et al. (2005) which is typical for tsunamigenic deposits (Goff et al., 2012; Spiske, 2020), whilst the presence of small pieces of gravel rules out aeolian deposition (Bondevik et al., 2005).

The samples from Dury Voe are comprised of fine to medium sands with a small silt component and have poor sorting values, with slightly better sorting at the landward site DV01. Distal samples are also finer than proximal samples, with mean grain size being 188 µm at DV01 *versus* 200 µm at DV08, which is consistent with a landward fining and sorting trend common in tsunami deposits (Goff et al., 2012; Spiske, 2020). The onshore deposit shows much higher mean grain sizes than offshore samples (with skeletal debris removed), suggesting that the finer fractions may have been carried further inland and/or were potentially removed by backwash flows after the individual waves.

The deposit shows a sharp, erosional lower contact and is discontinuous around DV01, both signatures typical of tsunami deposits (Dawson and Shi, 2000; Moore et al., 2011; Goff et al., 2012; Spiske, 2020). Overall, heavy-mineral composition of DV01 and DV08 is similar, with both being dominated by epidote and amphibole. On average, heavy minerals are more abundant closer to the shore (DV08) than landward (DV01), which reflects the change in flow speed and kinetic energy and is in accordance with observations from e.g., the 2011 Tohoku-oki tsunami deposits (Nakamura et al., 2012; Jagodziński et al., 2012).

5.2 Hydrodynamics of the tsunami based on internal variation of the deposit

5.2.1 Inferences from grain-size data

The presence of two distinct subunits in DV08 may support the assumption of two major, consecutive waves. The lower, massive to slightly coarsening-upward unit reflects highly concentrated flows, where frictional freezing reduces kinetic energy due to grain-grain collision and forces particles to settle (Spiske, 2020). The basal 1 cm of the deposit also shows the highest densities which seems common in non-normally graded sequences of tsunami deposits, where finer-grained and denser material settles first through kinetic sieving (Moore et al., 2011). The upper unit shows coarser grain sizes and a clearer coarsening-upward trend, which may be associated with transport in a traction carpet (Moore et al., 2011). A reverse trend of fining only occurs in the three uppermost samples indicating some decrease in hydrodynamics at the end of the sequence. This is supported by the fact that DV08 is located close (25 m) to the present-day shoreline, where turbulence, flow speed and kinetic energy are highest upon tsunami landfall. EMMA conducted on DV08 emphasises the difference between the two units as both are dominated by different EMs, while inverse grading in the upper unit is indicated by an incremental shift in EM ratios. EMMA was originally developed for unmixing of multimodal GSDs but achieves an adequate representation of the observed distinct subunits, indicating its potential for further application and facies separation on mainly unimodal GSDs.

Sedimentary features of core DV01 are less distinct but two subunits can still be differentiated from the grain-size data. Normal grading as identified in the lower sequence is associated with lower sediment concentration compared to DV08, inundation of moderate flow speeds up to stagnation and gravitational settling of the particles out of suspension (Goff et al., 2012; Jaffe et al., 2012; Spiske, 2020). Based on the position of DV01 c. 200 m inland, it seems likely that the sediment has been deposited out of suspension through gravitational settling in a phase of reduced flow speed during run-up as a result of the gently inclining topography and bottom friction. The normal grading is less pronounced in the upper sequence, potentially indicating that the sediment concentration was higher (Spiske, 2020). The upper unit appears massive to slightly fining upward, suggesting a higher sediment load or flow speed in a second wave, the latter in accordance with the observations of coarsening-up in core DV08.

5.2.2 Inferences from heavy-mineral data

In core DV08, the lower, massive unit shows the lowest heavy-mineral content towards the top. The upper, inversely graded unit associated with transport in a traction carpet shows low values at the lower boundary (depth c. 1.8 cm) which increase with particle size to up to 1.5 %, a pattern also documented in deposits of the 2011 Tohoku-oki tsunami, where the traction carpet also contained larger amounts of heavy minerals (Nakamura et al., 2012). However, the given heavy-mineral content by weight still contained quartz and feldspar contaminations that could not be removed during heavy-liquid separation. Especially the three topmost samples DV08/07-08, DV08/06 and DV08/05 were affected by this (20.87 %, 80.13 % and 39.56 % of grains were quartz or feldspar, respectively), making the heavy mineral concentration appear higher. Samples DV08/01–DV08/04 contained between 6.67–15.9 % contaminating quartz and feldspar grains. DV08/07-08 also has very few observations compared to the other samples, further limiting our confidence in the heavy mineral content of this sample. It is therefore assumed that the true increase in heavy minerals in the inversely graded sequence is not as steep as it appears. Nonetheless, these samples were retained in the analysis to preserve stratigraphic continuity and allow comparison across all core units, although their high quartz and feldspar content should be considered when interpreting the heavy mineral ratios.

At the boundary between the subunits of core DV08, a sharp increase in epidote and a sharp decrease in amphibole is observed. Across the upper subunit, amphibole shows a slight increasing trend towards the top. Cascalho et al. (2016) suggest that amphibole has a more platy (than rounded) shape which favours its slower deposition and further transport. This is only partly confirmed, as an increase in amphibole towards the top of the inversely graded unit is observed and the proximal core DV08 contains more amphibole overall than the distal core DV01. Mica settles later than other heavy minerals due to its platy shape (Costa and Dawson, 2022) and as such is concentrated in the uppermost millimetres of the upper unit of core DV08, where mean grain size also slightly decreases. This pattern likely reflects suspension grading during waning flow conditions. The high concentration of micas in these uppermost millimetres also leads to a certain bias indicating an overall slightly higher abundance of micas in the more proximal profile DV08. This observation diverges from the general landward increase reported in transects from the 2004 Indian Ocean tsunami deposit (Jagodziński et al., 2009).

There is less variability in the heavy mineral composition between the two subunits of the landward core DV01. Quartz and feldspar contamination is relatively even across all DV01 samples, at 7.64–16.76 % contaminating grains. Only sample DV01/09-10 contains 30.13 % contaminating grains, making the heavy mineral content appear higher. In the lower sequence of DV01, the mica content increases almost steadily as mean grain size decreases, in accordance with dominating deposition out of a suspension, where the smallest, lightest and/or platy shaped minerals settle last. Jagodziński et al. (2009) state that an absence of micas in the lower parts of a deposit is an indicator for bedload transport, whereas abundance of micas in the upper parts of the deposit indicates deposition from suspension.

5.3 Source area of the tsunami deposit

To better constrain the provenance of the tsunami deposit, we combined multivariate statistics supported by grain-size distributions, together with heavy-mineral analysis to integrate the compositional signals from both onshore and offshore samples. Costa et al. (2015) have investigated the sediment source of the Dury Voe event at Basta Voe using heavy mineral analysis and identified the beach and exposed glacial till as potential sources, whereas in this study we focus on the inter- to subtidal environments.

5.3.1 Grain size distributions and principal component analysis

Grain-size distributions analysed by end-member modelling (EMMA) (Figure 5) provide some evidence on transport processes and sediment sources. OFF10 has a maximum in the coarse silt to fine sand size range, overlapping best with DV01 and DV08. The relative scarcity of the finer fractions suggests that these were either transported further inland, as supported by observations from the 2011 Tohoku-Oki tsunami (Chagué et al., 2012; Matsumoto et al., 2023), or removed during the backwash. While grain-size patterns shed light on the transport and depositional processes, the analysis does not on its own constrain the source area of the tsunami deposit. To address provenance more directly, we applied principal component analysis (PCA) to the heavy mineral data.

Principal component analysis (PCA) of onshore and offshore data shows that PC1 and PC2 explain 54.6 % of the total variance in heavy mineral composition, capturing the dominant separation among samples. Higher-order components account for additional variance (Figure S8), which is typical for complex multivariate geochemical datasets.

Figure 8 separates the offshore samples into two groups: deeper-water sediments (OFF11–14), and shallower-water samples (OFF09–10), which cluster more closely with the onshore tsunami deposits (DV01, DV08) (Figure 8). Among these, OFF10 (14 m water depth) is mineralogically the most similar to the onshore core samples (DV01 and DV08) (Figure 8), supporting entrainment primarily from the intertidal to shallow subtidal zone down to ~14 m water depth rather than from deeper offshore sources. OFF09 (11 m) also shows a broadly similar heavy-mineral composition compared to the onshore deposits (DV01, DV08) (Figure 8). While PCA constrains the likely source area, more detailed insights into sediment provenance requires an examination of individual heavy-mineral ratios, together with an assessment of post-depositional weathering under acidic conditions.

5.3.2 Heavy mineral ratios and post-depositional weathering

To complement the PCA, which captures broad compositional variance, we examined heavy mineral ratios to obtain more detailed provenance signals and to test how reliably these are preserved under post-depositional alteration in the acidic peat environment (Figure 7). Both OFF09 (11 m) and OFF10 (14 m) show broadly similar mineral compositions to the onshore deposits (DV01 and DV08) (Figure 8).

Our results show that OFF10 contains large fractions of amphibole and epidote and similar proportions of mica and haematite as observed in DV01 and DV08. Moreover, OFF10 also contains 7 % spinel group minerals (titanomagnetite, magnetite, chromite), 5 % pyroxene and 3 % diopside, which are rare or absent in the onshore tsunami deposits (DV01 and DV08). In contrast to DV01, OFF10 has slightly more titanite, chloritoid and garnet, whereas these are absent or only found in small quantities onshore. OFF10 also shows markedly less tourmaline than the onshore deposits (DV01 and DV08). The onshore cores are enriched in tourmaline, especially in DV01, which likely reflects entrainment of intertidal and subtidal sediments enriched in tourmaline (>2 %) introduced from terrestrial sources i.e., via the creek. OFF09 differs from OFF10 mainly in spinel group minerals (titanomagnetite, magnetite, chromite; <1 %), garnet group (<1 %), and haematite group minerals (absent) but shows otherwise similar heavy mineral proportions.

The differences between onshore and offshore composition cannot be explained by source alone. The absence or depletion of pyroxene, diopside, titanite, garnet and minerals from the spinel group in the onshore deposits is more plausibly linked to post-depositional weathering and/or dissolution under acidic conditions (Figure S4), rather than their lack in the original source material. Experimental and field stability series (Bateman and Catt, 1985; Morton, 1985; Lång, 2000) consistently show that pyroxene, titanite and amphibole are relatively unstable in acidic environments, garnet, chloritoid and spinel have intermediate stability (garnet being the least stable among these three types under acidic conditions), whereas zircon, rutile and tourmaline are highly resistant (Table S6). The persistence of the resistant minerals in higher amounts in DV01 and DV08, together with the scarcity of the less stable ones, supports this post-depositional weathering interpretation. Thus, while ratios involving resistant minerals (e.g., zircon, tourmaline) may provide robust provenance information, ratios including unstable minerals cannot be straightforwardly interpreted in this low-pH setting. It is noteworthy that post-depositional weathering under acidic peat conditions (pH <4) greatly complicates the signal and limits the robustness of the multivariate statistical analysis.

The acidic setting at Dury Voe is further illustrated by the complete absence of carbonates in the tsunami deposits. Potential source deposits within the bay of Dury Voe contain abundant carbonate shells, shell fragments and foraminiferal tests (Figure S5), yet none were recovered from the tsunami deposits which appear to be carbonate-free. Humic acids percolating through the tsunami sands caused the full post-depositional dissolution of carbonates as also observed in tsunami deposits (e.g., Putra et al., 2023). Indeed, the dissolution of foraminiferal tests in marsh environments has been flagged as a major issue in foraminiferal research across the British Isles (Horton and Edwards, 2006).

Yawsangratt et al. (2012) observed that foraminiferal tests dissolved within 4.5 years after deposition by the 2004 Indian Ocean Tsunami, whilst similar carbonate dissolution has also been reported from tsunami deposits in temperate climates (Nanayama and Shigeno, 2006; Szczuciński et al., 2016). Attempts to reconstruct the foraminiferal assemblages of the tsunami deposit at Dury Voe using metagenomics (Engel et al., 2020) have not been successful (Patel et al., 2019), underscoring the severity of carbonate loss.

In summary, heavy mineral ratios reveal both provenance signals and the strong imprint of post-depositional weathering. Stable minerals such as tourmaline, rutile, and zircon remain reliable indicators of source, whereas unstable minerals and all carbonate phases have been lost. This constrains the resolution with which the source area can be defined and highlights the importance of integrating mineralogical evidence with the sedimentological data discussed above.

5.4 Timing and source of the tsunami

The tsunami deposit at Dury Voe has been dated to ~1500 cal yr BP by Bondevik et al. (2005) and correlated with deposits at Basta Voe, (Bondevik et al., 2005; Dawson et al., 2006) and Flugarth (Engel et al., 2024) in the Shetland Islands. The age-depth model at Flugarth (Hess et al., 2024) indicates a somewhat younger date within, however, a large error margin (1524–1163 cal yr BP or 426–787 CE, respectively) (Engel et al., 2024). The Flugarth dating is consistent with the two luminescence ages obtained in the present study which correspond to 470–650 CE (DV08-1) and 420–630 CE (DV08-2), respectively. Bayesian age modelling of all chronological evidence available from Shetland as described in section 3.7 identifies and constrains the age of the late Holocene Dury Voe tsunami at 470–630 CE (Figure 10, Table S4).

The robustness of the luminescence ages is supported by excellent agreement across multiple luminescence signals (quartz, IR_{50}, $pIRIR_{150}$) and aliquot sizes (SG, 1 mm, 2 mm, 8 mm) within 1σ uncertainties. This demonstrates that luminescence signals were sufficiently reset, provided that appropriate age models are used to isolate the best bleached grains.

A historical account from 720 AD, recorded at the monastery of Iona in western Scotland, describes an earthquake followed by a tsunami. Mac Conamhna (2023) linked this event to the Dury Voe deposit, but the lack of chronological overlap with the new modelled age estimate, geographically isolated sedimentary evidence and considerable distance between the sites make such a connection unlikely (Engel et al., 2024). Bondevik et al. (2005) instead suggested that the tsunami was triggered by a small, localised submarine landslide, although no candidate slump deposit has yet been identified on the seafloor around the Shetland Islands. At present, therefore, the trigger of the tsunami remains unknown.

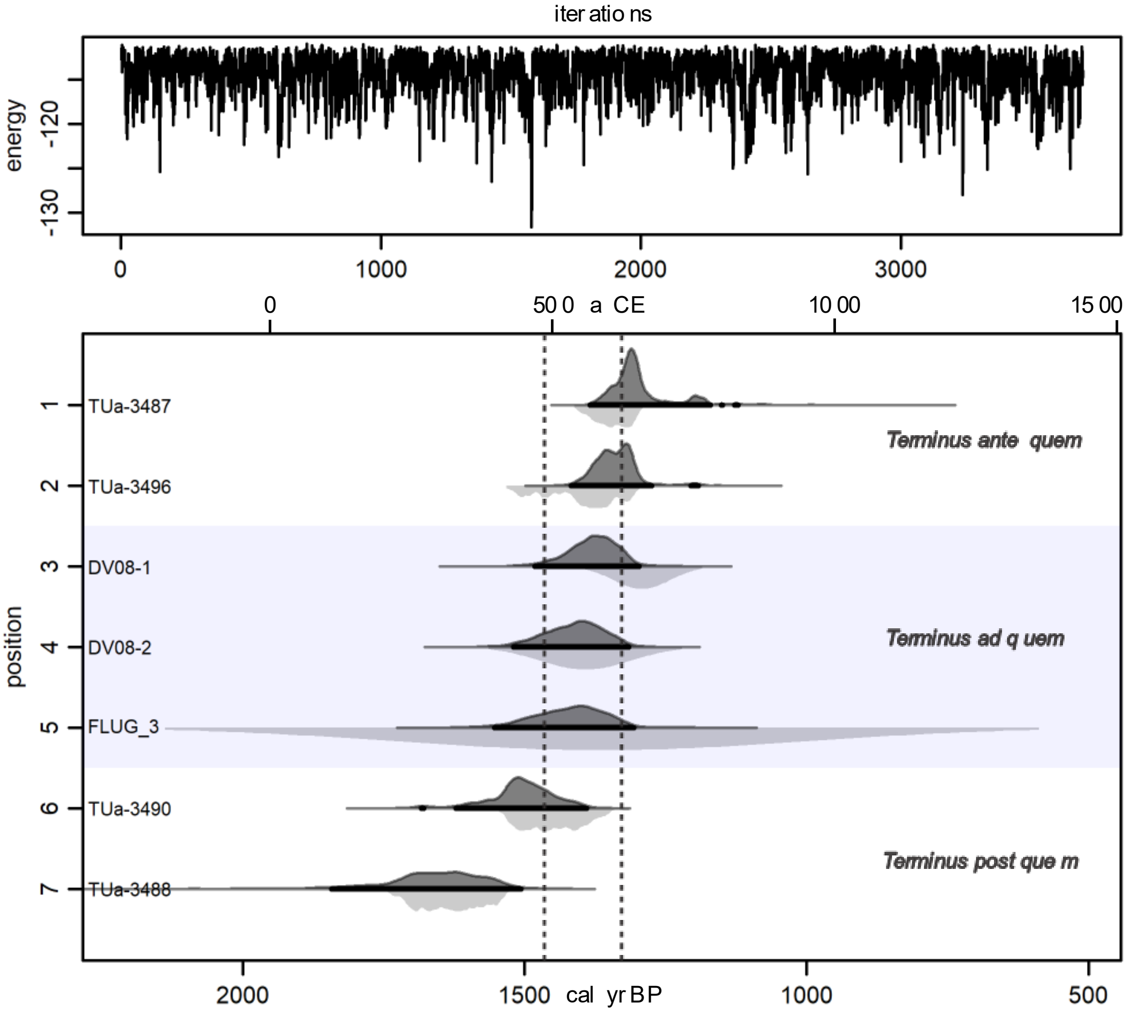

Figure 10. *Calibrated (light-grey 'reflections') and modelled ages (dark grey) with seven chronologically-ordered dated positions using the 'coffee' model (Blaauw et al., 2024). The dotted lines indicate the timespan between 1480–1320 cal yr BP (2σ) as the age range of the tsunami. The upper panel shows energy levels of the 3904 remaining MCMC iterations.*

6 Conclusion

High-resolution grain size and heavy mineral analyses, combined with Bayesian age modelling, provide new insights into the hydrodynamics, depositional patterns and sediment source area of palaeotsunami deposits on the Shetland Islands. The onshore palaeotsunami deposit of the Dury Voe event at both sampling sites comprises two subunits that correspond to at least two major inundating waves. Proximal deposits (to the shore) record high-velocity, high-density, bedload-dominated flows with a massive lower unit and an inversely graded upper unit. Distal to the shore, two less distinct, normally graded units are observed, reflecting reduced sediment load and flow velocity and energy causing suspension settling.

Shallow marine samples contain a stronger fine component (i.e., fine to medium sands) than onshore deposits, suggesting that this finer material was transported further inland (beyond the spatial extent of the sand) or removed by backwash. Heavy mineral assemblages reflect this inland gradient and closest similarity to modern intertidal and shallow subtidal sediments down to a water depth of 14 m bsl. This is consistent with mixing of shallow subtidal and intertidal materials, including creek-derived tourmaline-rich sand and gravel bars. However, post-depositional weathering in the highly acidic peat environment led to the dissolution of unstable heavy minerals and complete loss of carbonates (e.g., foraminiferal tests), leaving only stable minerals such as tourmaline, rutile and zircon as reliable provenance markers. Luminescence dating of both quartz and feldspar provides the first onshore ages for palaeotsunami deposits from the Shetland Islands. Our results place the Dury Voe event at 470–630 CE consistent with ages from Loch Flugarth, northern Mainland.

To further characterise the hydrodynamics at Dury Voe, future work should expand sampling across additional sites to integrate vertical patterns into a wider spatial context. Open questions remain about the trigger of the tsunami event. To address these questions, more locations along the eastern and northeastern coast should be investigated for traces of the event. Moreover, high-resolution offshore bathymetric mapping could be used to determine whether a potential slump deposit or submarine mass failure can be identified. Finally, to better resolve flow directions, anisotropy of magnetic susceptibility measurements within deposits are recommended. This study and work presented highlights the value of multi-proxy approaches and the complementarity between combined grain-size, multivariate, heavy mineral, Bayesian and luminescence methodologies. This work also serves as a reference for future palaeotsunami research especially for differentiating inundation phases and constraining the sediment source area.

Acknowledgements

The authors would like to acknowledge BELSPO who kindly funded the BRAIN-be proposal “GEN-EX” (BR/175/PI/GEN-EX). We acknowledge the possibility for Geotek core logging at Renard Center of Marine Geology, Ghent University, and the support by Evelien Boes. Julien Cillis (Institute of Natural Sciences, Brussels) is thanked for taking the SEM images. Nicola Manke supported the density separation of heavy minerals. The access to private lands around Dury Voe was kindly granted by local landowners.

Competing interests

None of the authors has any competing interests to declare.

Author contributions

NN: methodology (equal), investigation (equal), visualisation (lead), writing – original draft (lead), writing – review and editing (equal); ME: Conceptualization (lead), fieldwork (equal), project administration (equal), methodology (equal), investigation (supporting), writing – original draft (supporting), writing – review and editing (equal); TP: fieldwork (equal), investigation (supporting), writing – original draft (supporting); writing – review and editing (equal); AV: methodology (equal), investigation (equal), writing – review and editing (equal); HPM: methodology (equal), writing – review and editing (equal); DB: methodology (equal), investigation (equal), writing – review and editing (equal); AP: investigation (supporting), writing – review and editing (equal); PK: fieldwork (equal), writing – review and editing (equal); KH: methodology (equal), writing – review and editing (equal); IS: Funding acquisition (equal), project administration (equal), writing – review and editing (equal); VMAH: Fieldwork (equal), funding acquisition (equal), project administration (equal), writing – review and editing (equal); SD: Conceptualization (supporting), fieldwork (equal), writing – review & editing (equal).

Funding Statement

The study was funded by Belgian Science Policy Belspo (BR/175/PI/GEN-EX). For the publication fee we acknowledge financial support by Deutsche Forschungsgemeinschaft within the funding programme “Open Access Publikationskosten” and by Heidelberg University.

Data availability statement

Data reported here are stored at heiDATA https://doi.org/10.11588/XYZ and are freely accessible under a Creative Commons Attribution 4.0 International Licence (CC BY 4.0). Correspondence and requests for materials should be addressed to NN. This study does not use custom code or a mathematical algorithm that is deemed central to the conclusions

References

Bateman, RM and Catt JA (1985) Modification of heavy mineral assemblages in English coversands by acid pedochemical weathering. *Catena* 12: 1–21. https://doi.org/10.1016/S0341-8162(85)80001-1

Blaauw M, Aquino-López M, Christen JA (2024) Modelling chronologically ordered radiocarbon dates in R. *Radiocarbon*. https://doi.org/10.1017/RDC.2024.56

Blott SJ and Pye K (2001) GRADISTAT: a grain size distribution and statistics package for the analysis of unconsolidated sediments. *Earth Surface Processes and Landforms* 26: 1237–1248. https://doi.org/10.1002/esp.261

Boenigk W (1983) *Schwermineralanalyse*. Stuttgart: Enke.

Bondevik S, Mangerud J, Dawson S, Dawson A and Lohne Ø (2003) Record-breaking height for 8000-year-old tsunami in the North Atlantic. *EOS* 84: 289–293. https://doi.org/10.1029/2003EO310001

Bondevik S, Mangerud J, Dawson S, Dawson A and Lohne Ø (2005) Evidence for three North Sea tsunamis at the Shetland Islands between 8000 and 1500 years ago. *Quaternary Science Reviews* 24: 1757–1775. https://doi.org/10.1016/j.quascirev.2004.10.018

Bondevik S, Stormo SK and Skjerdal G (2012) Green mosses date the Storegga tsunami to the chilliest decades of the 8.2 ka cold event. *Quaternary Science Reviews* 45: 1–6. https://doi.org/10.1016/j.quascirev.2012.04.020

Bradwell T, Small D, Fabel D, Clark CD, Chiverrell RC, Saher MH, Dove D, Callard SL, Burke MJ, Moreton SG, Medialdea A, Bateman MD, Roberts DH, Golledge NR, Finlayson A, Morgan S and Cofaigh CÓ (2021) Pattern, style and timing of British–Irish Ice Sheet retreat: Shetland and northern North Sea sector. *Journal of Quaternary Science* 36: 681–722. https://doi.org/10.1002/jqs.3163

Brill D and Tamura T (2020) Optically stimulated luminescence dating of tsunami and storm deposits. In: Engel M, Pilarczyk J, May SM, Brill D, Garrett EG (eds) *Geological Records of Tsunamis and Other Extreme Waves*. Amsterdam: Elsevier, pp.705–727. https://doi.org/10.1016/B978-0-12-815686-5.00032-8

Brill D, Reimann T, Wallinga J, May SM, Engel M, Riedesel S and Brückner H (2018) Testing the accuracy of feldspar single grains to date late Holocene cyclone and tsunami deposits. *Quaternary Geochronology* 48: 91–103. https://doi.org/10.1016/j.quageo.2018.09.001

Cascalho J, Costa PJM, Dawson S, Milne F, and Rocha A (2016) Heavy mineral assemblages of the Storegga tsunami deposit. *Sedimentary geology* 334: 21–33. https://doi.org/10.1016/j.sedgeo.2016.01.007.

Chagué-Goff C, Andrew A, Szczuciński W, Goff J, and Nishimura Y (2012) Geochemical signatures up to the maximum inundation of the 2011 Tohoku-oki tsunami – implications for the 869 AD Jogan and other palaeotsunamis. *Sedimentary Geology* 282: 65–77. https://doi.org/10.1016/j.sedgeo.2012.05.021

Clark CD, Ely JC, Hindmarsh RCA, Bradley S, Ignéczi A, Fabel D, Ó Cofaigh C, Chiverrell RC, Scourse J, Benetti S, Bradwell T, Evans DJA, Roberts DH, Burke M, Callard SL, Medialdea A, Saher M, Small D, Smedley RK, Gasson E, Gregoire L, Gandy N, Hughes ALC, Ballantyne C, Bateman MD, Bigg GR, Doole J, Dove D, Duller GAT, Jenkins GTH, Livingstone SL, McCarron S, Moreton S, Pollard D, Praeg D, Sejrup HP, Van Landeghem KJJ and Wilson P (2022) Growth and retreat of the last British–Irish Ice Sheet, 31 000 to 15 000 years ago: the BRITICE-CHRONO reconstruction. *Boreas* 51: 699–758. https://doi.org/10.1111/bor.12594

Costa PJM, Andrade C, Cascalho J, Dawson AG, Freitas MC, Paris R and Dawson S (2015) Onshore tsunami sediment transport mechanisms inferred from heavy mineral assemblages. *The Holocene* 25: 795–809. https://doi.org/10.1177/09596836155693

Costa PJM, Dawson S, Ramalho R, Engel M, Dourado F, Bosnic I and Andrade C (2021) A review on onshore tsunami deposits along the Atlantic coasts. *Earth-Science Reviews* 212: 103441. https:// doi.org/10.1016/j.earscirev.2020.103441

Dawson AG and Shi S (2000) Tsunami Deposits. *Pure and Applied Geophysics* 157: 875–897. https://doi.org/10.1007/s000240050010

Dawson AG, Dawson S and Bondevik S (2006) A Late Holocene Tsunami at Basta Voe, Yell, Shetland Isles. *Scottish Geographical Journal* 122: 100–108. https://doi.org/10.1080/00369220600917404

Dawson AG, Dawson S, Bondevik S, Costa PJM, Hill J and Stewart I (2020) Reconciling Storegga tsunami sedimentation patterns with modelled wave heights: A discussion from the Shetland Isles field laboratory. *Sedimentology* 67: 1344–1353. https://doi.org/10.1111/sed.12643

Dietze E and Dietze M (2019) Grain-size distribution unmixing using the R package EMMAgeo. *E&G Quaternary Science Journal* 68: 29–46. https://doi.org/10.5194/egqsj-68-29-2019

Durcan JA, King GE and Duller GAT (2015) DRAC: dose rate and age calculator for trapped charge dating. *Quaternary Geochronology* 28: 54–61. https://doi.org/10.1016/j.quageo.2015.03.012

Engel M, May SM, Pilarczyk J, Brill D and Garrett E (2020) Geological records of tsunamis and other extreme waves: concepts, applications and a short history of research. In: Engel M, Pilarczyk J, May SM, Brill D and Garrett E (eds) *Geological records of tsunamis and other extreme waves*. Amsterdam: Elsevier, pp.3–20. https://doi.org/10.1016/B978-0-12-815686-5.00001-8

Engel, M., Schön, I., Patel, T., Pawłowski, J., Szczuciński, W., Dawson, S., Garrett, E., Heyvaert, V.M.A., 2020. Paleogenetic approach in tsunami deposit studies. In: Engel, M., Pilarczyk, J., May, S.M., Brill, D., Garrett, E. (eds.), *Geological records of tsunamis and other extreme waves*. Amsterdam: Elsevier, pp.427–442. https://doi.org/10.1016/B978-0-12-815686-5.00020-1

Engel M, Hess K, Dawson S, Patel T, Koutsodendris A, Vakhrameeva P, Klemt E, Kempf P, Schön I and Heyvaert VMA (2024) Sedimentary evidence of the Late Holocene tsunami in the

Shetland Islands (UK) at Loch Flugarth, northern Mainland. *Boreas* 53: 27–41. https://doi.org/10.1111/bor.12635

Firth CR and Smith DE (1993) Holocene Sea-Level Changes in Shetland. In: Birnie J, Gordon J, Bennett K and Hall A (eds) *The Quaternary of Shetland. Field guide*. London: Quaternary Research Association, p.17.

Folk RL and Ward WC (1957) Brazos River bar: a study in the significance of grain size parameters. *Journal of Sedimentary Petrology* 27: 3–26. https://doi.org/10.1306/74D70646-2B21-11D7-8648000102C1865D

Galbraith RF, Roberts RG, Laslett GM, Yoshida H, Olley JM (1999) Optical dating of single and multiple grains of quartz from Jinmium Rock Shelter, Northern Australia: Part I, experimental design and statistical models. *Archaeometry* 41: 339–364. https://doi.org/10.1111/j.1475-4754.1999.tb00987.x

Gillen C (2003) *Geology and Landscapes of Scotland*. Harpenden: Terra.

Goff J, Chagué-Goff C, Nichol S, Jaffe B and Dominey-Howes D (2012) Progress in palaeotsunami research. *Sedimentary Geology* 243–244: 70–88. https://doi.org/10.1016/j.sedgeo.2011.11.002

Guérin G, Mercier N and Adamiec G (2011) Dose-rate conversion factors: Update. *Ancient TL* 29: 5–8. https://doi.org/10.26034/la.atl.2011.443

Hall AM, Hansom JD and Gordon JE (2021) Shetland. In: Ballantyne CK and Gordon JE (eds) *Landscapes and Landforms of Scotland*. Cham: Springer, pp.135–150. https://doi.org/10.1007/978-3-030-71246-4_7

Hesemann M (2015) The foraminifera.eu database: concept and status. *Palaeontologica Electronica* 18: 48A. https://doi.org/10.26879/154E

Hess K, Engel M and Koutsodendris A (2023) Sedimentological storm and tsunami record of Loch Flugarth, Shetland Islands (UK). heiDATA. https://doi.org/10.11588/data/QJEZHT

Hess K, Engel M, Patel T, Vakhrameeva P, Koutsodendris A, Klemt E, Hansteen TH, Kempf P, Dawson S, Schön I and Heyvaert VMA (2024) A 1500-years record of North Atlantic storm flooding from lacustrine sediments, Shetland Islands (UK). *Journal of Quaternary Science* 39: 37–53. https://doi.org/10.1002/jqs.3568

Horton BP and Edwards RJ (2006) Quantifying Holocene sea-level change using intertidal foraminifera: lessons from the British Isles. *Cushman Foundation for Foraminiferal Research, Special Publication* 40: 1–97.

Huntley DJ and Lamothe M (2001) Ubiquity of anomalous fading in K-feldspars and the measurement and correction for it in optical dating. *Canadian Journal of Earth Sciences* 38: 1093–1106. https://doi.org/10.1139/e01-013

IOC (Intergovernmental Oceanographic Commission) (2019) Tsunami glossary 2019. *IOC Technical Series* 85: 6–42.

Jagodziński R, Sternal B, Szczuciński W and Lorenc S (2009) Heavy minerals in 2004 tsunami deposits on Kho Khao Island, Thailand. *Polish Journal of Environmental Studies* 18: 103–110.

Jagodziński R, Sternal B, Szczuciński W, Chagué-Goff C. and Sugawara D (2012) Heavy minerals in the 2011 Tohoku-oki tsunami deposits—insights into sediment sources and hydrodynamics. *Sedimentary Geology* 282: 57–64. http://dx.doi.org/10.1016/j.sedgeo.2012.07.015

Jaffe B, Goto K, Sugawara D, Richmond BM, Fujino S and Nishimura Y (2012) Flow speed estimated by inverse modeling of sandy tsunami deposits: results from the 11 March 2011 tsunami on the coastal plain near the Sendai Airport, Honshu, Japan. *Sedimentary Geology* 282: 90–109. https://doi.org/10.1016/j.sedgeo.2012.09.002

Jolliffe IT and Cadima J (2016) Principal component analysis: A review and recent developments. *Philosophical Transactions of the Royal Society of London, Series A: Mathematical, Physical, and Engineering Sciences* 374, 20150202. https://doi.org/10.1098/rsta.2015.0202

Kreutzer S, Schmidt C, DeWitt R and Fuchs M (2014) The a-value of polymineral fine grain samples measured with the post-IR IRSL protocol. *Radiation Measurements* 69, 18–29. https://doi.org/10.1016/j.radmeas.2014.04.027

Lång L-O (2000) Heavy mineral weathering under acidic soil conditions. *Applied Geochemistry* 15: 415–423. https://doi.org/10.1016/S0883-2927(99)00064-5

Mac Conamhna OAP (2023) A seismic tsunami in the Irish annals, recorded at Iona in October 720. *Marine Geology* 456, 106973. https://doi.org/10.1016/j.margeo.2022.106973

Matsumoto D, Sawai Y, Tanigawa, K, Namegaya Y, Shishikura M, Kagohara K, Fujiwara O and Shinozaki T (2023) Sedimentary diversity of the 2011 Tohoku-oki tsunami deposits on the Sendai coastal plain and the northern coast of Fukushima Prefecture, Japan. *Progress in Earth and Planetary Sciences* 10: 23. https://doi.org/10.1186/s40645-023-00553-3

Moore A, Goff J, McAdoo BG, Fritz HM, Gusman A, Kalligeris N, Kalsum K, Susanto A, Suteja D. and Synolakis CE (2011) Sedimentary deposits from the 17 July 2006 western Java tsunami, Indonesia: use of grain size analyses to assess tsunami flow depth, speed, and traction carpet characteristics. *Pure and Applied Geophysics* 168: 1951–1961. https://doi.org/10.1007/s00024-011-0280-8

Morton AC (1985) Heavy minerals in provenance studies. In: Zuffa GG (ed) *Provenance of Arenites*. Dordrecht: Springer, pp.249–277. https://doi.org/10.1007/978-94-017-2809-6_12

Murray AS and Wintle AG (2000) Luminescence dating of quartz using an improved single-aliquot regenerative-dose protocol. *Radiation Measurements* 32: 57–73. https://doi.org/10.1016/S1350-4487(99)00253-X

Nakamura Y, Nishimura Y and Putra PS (2012) Local variation of inundation, sedimentary characteristics, and mineral assemblages of the 2011 Tohoku-oki tsunami on the Misawa coast, Aomori, Japan. *Sedimentary Geology* 282: 216–227. https://doi.org/10.1016/j.sedgeo.2012.06.003

Nanayama F and Shigeno K (2006) Inflow and outflow facies from the 1993 tsunami in southwest Hokkaido. *Sedimentary Geology* 187: 139–158. https://doi.org/10.1016/j.sedgeo.2005.12.024

Nielsen F (2016) *Introduction to HPC with MPI for Data Science*. Cham: Springer. https://doi.org/10.1007/978-3-319-21903-5

Patel T, Engel M, Dawson S, Pint A, Garrett E, Szczucinski W, Kempf P, Schön I and Heyvaert, VMA (2019) *Metagenomics of tsunami deposits using eDNA: first results from the Shetland Islands, U.K.* 20th INQUA Congress, Dublin, Ireland, 25–31 July 2019, Abstract #2691.

Prescott JR and Hutton JT (1994) Cosmic ray contributions to dose rates for luminescence and ESR dating: Large depths and long-term time variations. *Radiation Measurements* 23: 497–500. https://doi.org/10.1016/1350-4487(94)90086-8

Putra PS, Yulianto E and Nugroho SH (2023) Distribution patterns of foraminifera in paleotsunami layers: A review. *Natural Hazards Research* 3: 1–13. https://doi.org/10.1016/j.nhres.2022.12.004

Riedesel S, Autzen M and Burow, C (2019) scale_GammaDose( ): calculate the gamma dose deposited within a sample taking layer-to-layer variations in radioactivity into account (according to Aitken, 1985). Function version 0.1.1. In: Kreutzer S, Burow C, Dietze M, Fuchs MC, Schmidt C, Fischer M, and Friedrich J (eds) *Luminescence: Comprehensive Luminescence Dating Data Analysis. R package version 0.9.0.87*. https://doi.org/10.32614/CRAN.package.Luminescence

Smedley RK, Duller G, Pearce N and Roberts H (2012) Determining the K-content of single-grains of feldspar luminescence dating. *Radiation Measurements* 47: 790–796. https://doi.org/10.1016/j.radmeas.2012.01.014

Smith J (1993) Introduction to the Coastal Geomorphology. In: Birnie J, Gordon J, Bennett K and Hall A (eds) *The Quaternary of Shetland. Field guide*. London: Quaternary Research Association, pp.4–5.

Spiske M (2020) The sedimentology and geometry of fine-grained tsunami deposits from onshore environments. In: Engel M, Pilarczyk J, May SM, Brill D and Garrett E (eds) *Geological records of tsunamis and other extreme waves*. Amsterdam: Elsevier, 213–238. https://doi.org/10.1016/B978-0-12-815686-5.00011-0

Szczuciński W, Pawłowska J, Lejzerowicz F, Nishimura Y, Kokociński M, Majewski W, Nakamura Y and Pawłowski J (2016) Ancient sedimentary DNA reveals past tsunami deposits. *Marine Geology* 381: 29–33. https://doi.org/10.1016/j.margeo.2016.08.006

Weiss R and Bourgeois J (2012) Understanding sediments – reducing tsunami risk. Science 336: 1117–1118. https://doi.org/10.1126/science.1221452

WoRMS Editorial Board (2025) World Register of Marine Species. https://doi.org/10.14284/170

Yawsangratt S, Szczuciński W, Chaimanee N, Chatprasert S, Majewski W and Lorenc S (2012) Evidence of probable paleotsunami deposits on Kho Khao Island, Phang Nga Province, Thailand. *Natural Hazards* 63: 151–163. https://doi.org/10.1007/s11069-011-9729-4

Late Holocene tsunami hydrodynamics, sediment provenance and chronology from Dury Voe, Shetland Islands (UK)

Nel NUSSBERGER[1], Max ENGEL[1,2], Tasnim PATEL[3], Alexander VARYCHEV[4], Hans-Peter MEYER[4], Dominik BRILL[5], Anna PINT[6], Philipp KEMPF[2], Katharina HESS[1], Isa SCHÖN[7,8], Vanessa M.A. HEYVAERT[2,9], Sue DAWSON[10]

[1]*Heidelberg University, Institute of Geography, Heidelberg, Germany*

[2]*Institute of Natural Sciences, Geological Survey of Belgium, Brussels, Belgium*

[3]*Institute of Natural Sciences, MARECO, Marine Ecology and Management, Brussels, Belgium*

[4]*Heidelberg University, Institute of Earth Sciences, Heidelberg, Germany*

[5]*University of Cologne, Institute of Geography, Cologne, Germany*

[6]*University of Hamburg, Institute for Geology, Hamburg, Germany*

[7]*Institute of Natural Sciences, ATECO, Freshwater Biology, Brussels, Belgium*

[8]*University of Hasselt, Research Group Zoology, Campus Diepenbeek, Diepenbeek, Belgium*

[9]*Ghent University, Department of Geology, Ghent, Belgium*

[10]*University of Dundee, Division of Energy, Environment & Society, Dundee, Scotland*

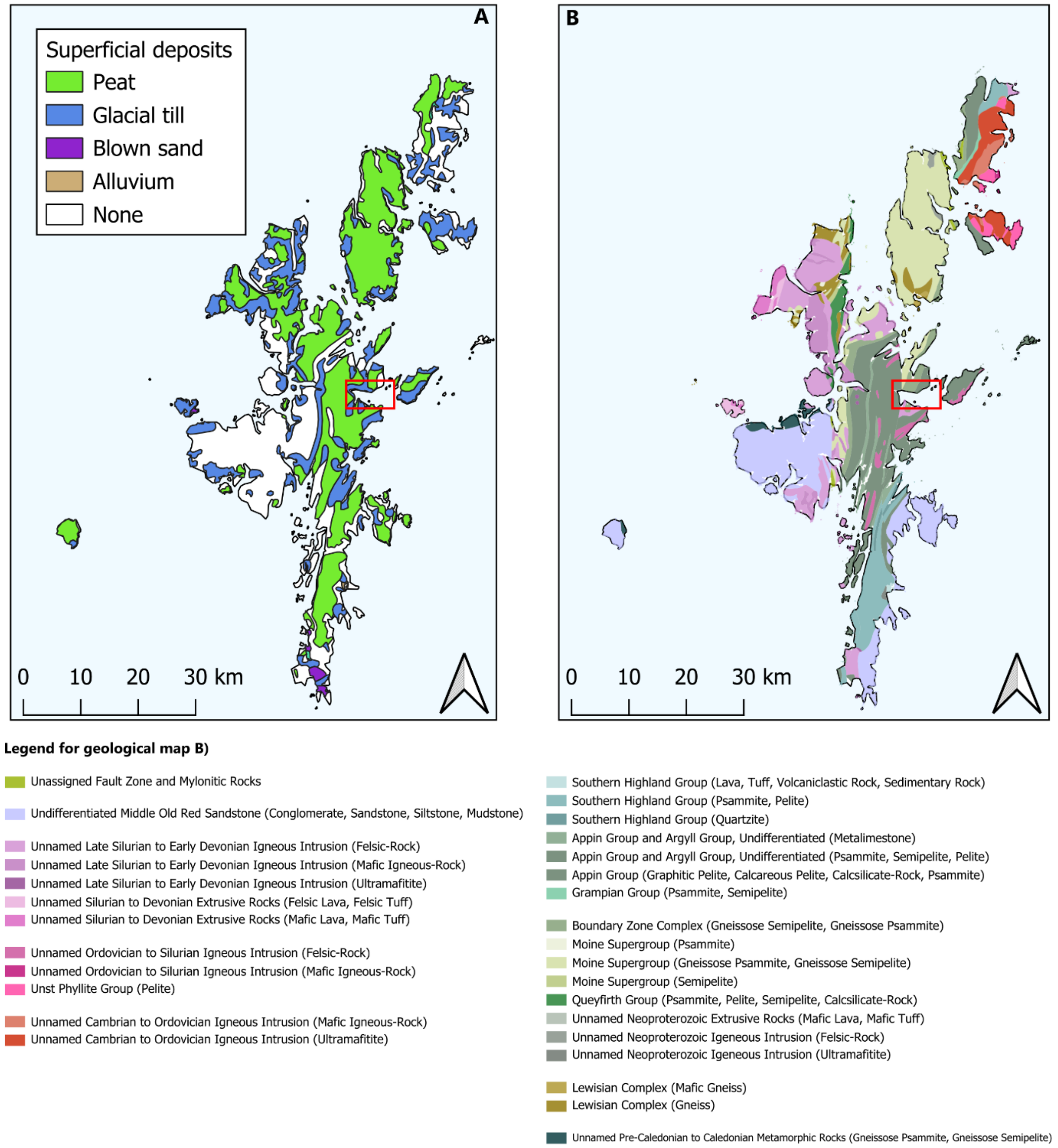

Figure S1. Map of superficial deposits (A) and bedrock geology (B) of the Shetland islands (based on British Geological Survey materials © UKRI 2025), with the study site of Dury Voe marked in a red frame (Figure 2A, main text).

Table S1. Environmental dose rates for the luminescence samples.

Sample	Lab-ID	Depth (m)	U (ppm)	Th (ppm)	K (%)	Water (%)	Dose rate (Gy/ka)
DV08 Peat	-	0.4–0.6	0.78±0.07	3.68±0.25	1.10±0.02	130±10	
DV08-2	C-L5105, C-L5106	0.63	1.18±0.09	3.81±0.28	1.87±0.05	30±10	1.74±0.12 (Q) 2.40±0.17 (F)

Table S2. Quartz OSL (left) and feldspar pIRIR$_{150}$ (right) dating protocols.

Step	Treatment	Signal
1	Preheat (220 °C for 10 s)	
2	Blue LEDs (40 s @ 125 °C)	Lx (OSL)
3	Test dose	
4	Cutheat (200 °C)	
5	Blue LEDs (40 s @ 125 °C)	Tx (OSL)
6	Dose (R1-R4, R0, RR, DR)	
7	Return to step 1	

R1-x = regeneration doses, R0 = zero dose
RR = recycling dose, DR = depletion ratio

Step	Treatment	Signal
1	Preheat (175 °C for 60 s)	
2	IRSL LEDs (200 s @ 50 °C)	Lx (IRSL)
3	IRSL LEDs (300 s @ 150 °C)	Lx (pIRIR)
3	Test dose	
4	Preheat (175 °C for 60 s)	
5	IRSL LEDs (200 s @ 50 °C)	Tx (IRSL)
6	IRSL LEDs (300 s @ 150 °C)	Tx (pIRIR)
7	Dose (R1-R4, R0, RR)	
8	Return to step 1	

Table S3. ^{14}C data of relevant samples from stratigraphic sections at Basta Voe (BV) and Dury Voe (DV) containing tsunami deposits of the Dury Voe event. The data and sample information were taken from Bondevik et al. (2005) and recalibrated using the most recent IntCal20 calibration curve (Reimer et al., 2020) for this table.

Lab no.	Site	Material	Vertical location	δ^{13}C	^{14}C age (BP)	Error	Age in cal. a **BCE**/CE (2σ)	Age in cal. a BP (2σ)
TUa-3487	DV	Plant fragments: 9 seeds, 2 catkin scales, 1 fragment of charcoal, 1 fragment of bark >1 mm + many small fragments (0.5–1 mm) of charcoal, twigs and insects (14.7 mg)	1–2 cm above upper boundary of the sand layer	-28.1	1460	± 50	423–663	1507–1287
TUa-3488	DV	Plant fragments: 10 charcoal fragments, 4 fragments of insects >1 mm. In addition, many small fragments (0.5–1 mm) of charcoal, twigs and insects (25.6 mg)	1–2 cm below the lower boundary of the sand layer	-28.8	1745	± 60	132–430	1818–1520
TUa-3489	DV	Plant fragments: 7 small charcoal fragments, 4 fragments of insects, small twigs and bark fragments (10.5 mg)	7–8 cm below the lower boundary of the sand layer	-29.7	2105	± 55	**353**–23	2303–1927
TUa-3490	BV	Plant fragments: 3 twigs (possibly *Calluna* sp.) with bark; (a) 2 mm x 15 mm, (b) 1.5 mm x 12 mm and (c) 2 mm x 20 mm. Tiny roots were removed (22.9 mg)	0–1 cm below the lower boundary of the sand layer	-28.6	1570	± 55	404–605	1546–1345
TUa-3496	BV	Plant fragments: 3 twigs (possibly *Calluna* sp.) with bark; (a) 10 mm x 2 mm with bark, (b) 5 mm x 3 mm with bark and (c) 1 mm x 2 mm. Tiny roots were removed (18.0 mg)	5 cm above the upper boundary of the sand layer	-27.8	1505	± 60	433–647	1517–1303

Table S4. Ages derived by the Bayesian age model ‘coffee’ Blaauw et al. (2024). All statistical ages refer to the cal yr BP scale (before AD 1950). 85.37 % of the modelled ages fall within the 95 % highest posterior density ranges of the unmodelled dates.

ID	Min95	Max95	Median	Mean	Mode	Type	Interpretation	Source
TUa–3487	1106	1367	1309	1292	1311	^{14}C-AMS	*Terminus ante quem*	Bondevik et al. (2005); see Table S3
TUa–3496	1215	1404	1340	1337	1320	^{14}C-AMS	*Terminus ante quem*	Bondevik et al. (2005); see Table S3
DV08–1	1298	1481	1376	1379	1376	Luminescence age	*Terminus ad quem*	This study
DV08–2	1323	1522	1407	1413	1399	Luminescence age	*Terminus ad quem*	This study
FLUG_3	1313	1556	1415	1420	1401	Derived from age-depth model	*Terminus ad quem*	Hess et al. (2023, 2024)
TUa–3490	1403	1664	1503	1506	1511	^{14}C-AMS	*Terminus post quem*	Bondevik et al. (2005); see Table S3
TUa–3488	1523	1859	1650	1657	1624	^{14}C-AMS	*Terminus post quem*	Bondevik et al. (2005); see Table S3

Table S5. Location and water depths of modern surface samples (bmsl=below mean sea level; WD=water depth).

Sample	North	Longitude	WD (m bmsl)	Comments
OFF09	60.331559N	1.170389W	11.0	Inside Dury Voe; muddy sand, dark brown, well sorted
OFF10	60.335952N	1.170595W	14.0	Inside Dury Voe muddy sand, dark brown, moderately sorted, dominated by shell debris
OFF11	60.33779N	1.165084W	24.0	Inside Dury Voe; muddy sand, dark brown, moderately to well sorted
OFF12	60.341278N	1.160139W	31.0	Inside Dury Voe; sandy mud, dark brown, moderately to well sorted
OFF13	60.343004N	1.152824W	37.0	Inside Dury Voe; sandy mud, dark brown, moderately to well sorted
OFF14	60.341574N	1.135403W	42.5	Inside Dury Voe; sandy, more poorly sorted, entire small mollusk shell, only small amount of amount of material retrieved
OFF15	60.376331N	1.126952W	10.0	Near Vidlin marina; sandy, many skeletal grains, green macroalgae
DVM01	60.3272N	1.16801W	1.1	Uppermost subtidal, innermost Dury Voe
DVM02	60.3249N	1.1687502W	-	Intertidal, medium to coarse sand, behind the gravel barrier
DVM03	60.323619N	1.166397W	-	Intertidal, close to DV08
DVM04	60.326299N	1.168181W	0.8	Uppermost subtidal, innermost Dury Voe

Table S6. Heavy mineral groupings and density ranges based on Mange and Maurer (1991), with additions from Klein and Hurlbut (1985)[2], Anthony et al. (no date)[3], and Leveneur et al. (2021)[4]. Diopside is a calcium-rich clinopyroxene (Mange and Maurer, 1991) but was not sorted into the pyroxene group since it was present in substantial quantities and other identified pyroxenes are only classified as ortho- or clinopyroxenes, not more detailed. In the case of the garnet group, most observations were of generic garnets and grossular showed only a few counts and was therefore grouped with the garnets. Across all samples, a total of 10475 grains were identified. Two total observations of chalcopyrite, one of åkermanite, and three of chlorite were grouped as "others" (together with grains whose minerals could not be identified or artefacts from sample preparation, e.g., grains from polishing paste) and excluded from further analysis.

Group	**Minerals**	**Density [g/cm³]**
Al_2SiO_5 group	Andalusite	3.13–3.16
	Staurolite	3.74–3.83
Amphibole group	Hornblende	3.02–3.5
	Actinolite	3.02–3.44
	Tremolite	3.02–3.44
	Unspecified amphiboles	?
Chloritoid	Chloritoid	3.51–3.8
Diopside	Diopside	3.22–3.38
Epidote group	Epidote	3.38–3.49
	Zoisite	3.15–3.27
	Allanite	3.4–4.2
	Epidote mix	?
Garnet group	Garnet	3.4–4.3
	Grossular	3.4–3.6
Haematite group	Ilmenite	4.7[2]
	Pyrophanite	4.54[3]
Mica group	Muscovite	2.77–2.88
	Biotite	2.7–3.3
	Margarite	3.0–3.1[2]
Phosphate group	Monazite	5.0–5.3
	Xenotime	4.59
Pyroxene group	Orthopyroxene	~3.21
	Clinopyroxene	2.96–3.52
Rutile	Rutile	4.23–5.5
Spinel group	Magnetite	5.18[2]
	Titanomagnetite	5.1[4]
	Chromite	4.6[2]
Titanite	Titanite	3.45–3.55
Tourmaline	Tourmaline	3.0–3.25
Zircon	Zircon	4.6–4.79

Figure S3 (above). Full extent of core DV08.

Figure S2 (left). Full extent of core DV01.

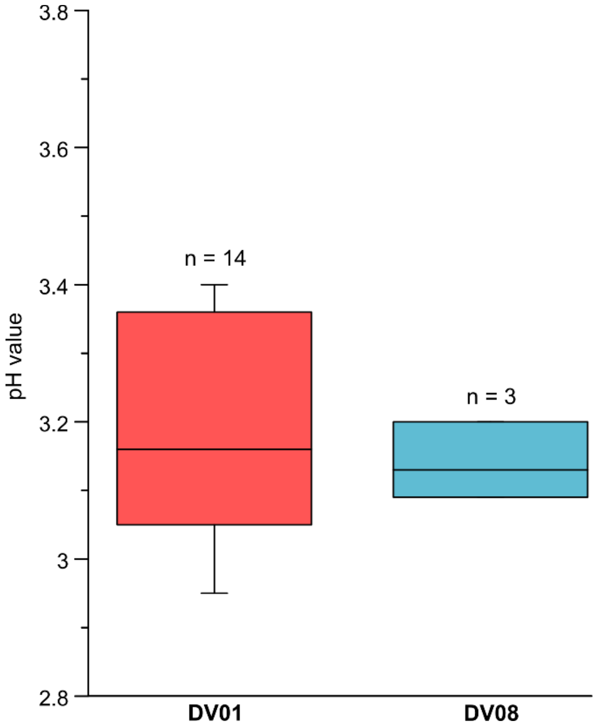

Figure S4. pH values of peat samples above and below the tsunami deposit in cores DV01 and DV08 from Dury Voe site, reflecting a high acidity of the sedimentary environment.

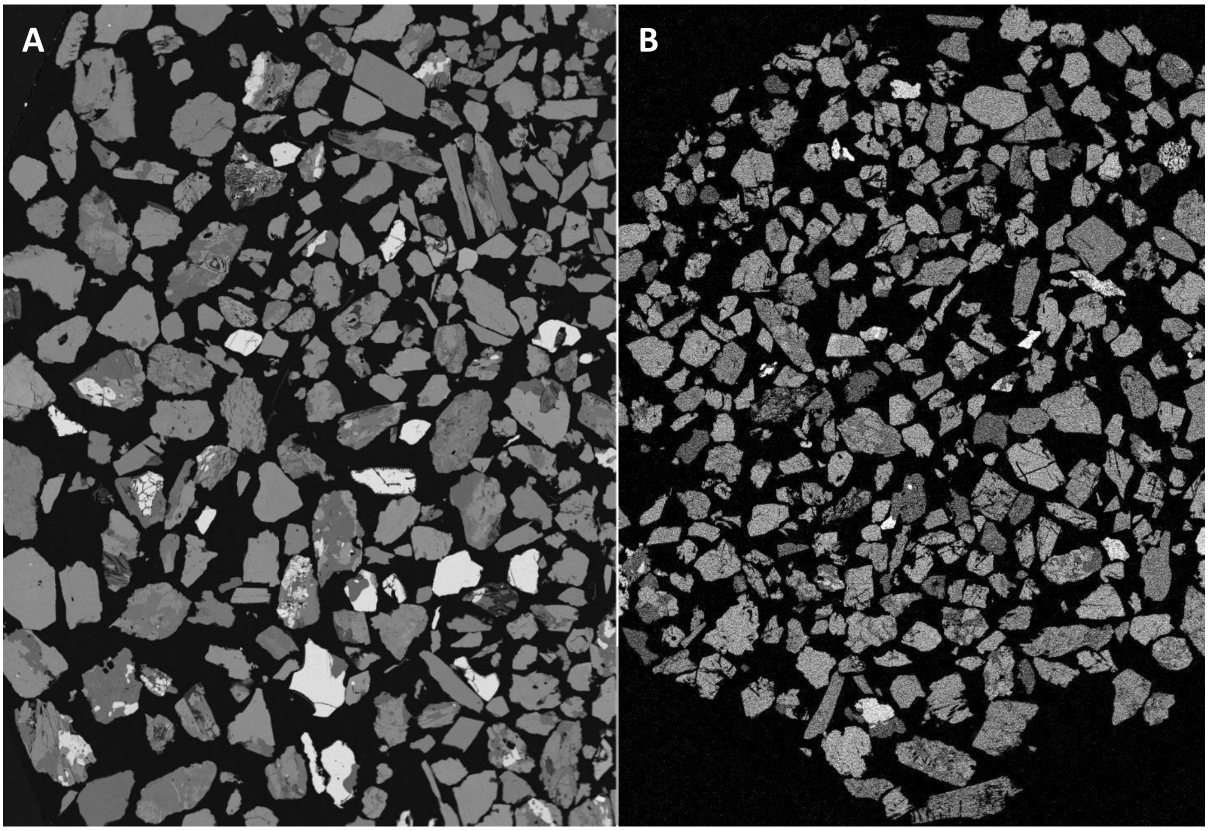

Figure S5. Electron microscopy picture of analysed heavy mineral grains from A) offshore sample OFF10 and B) onshore sample DV08/03, from Dury Voe site.

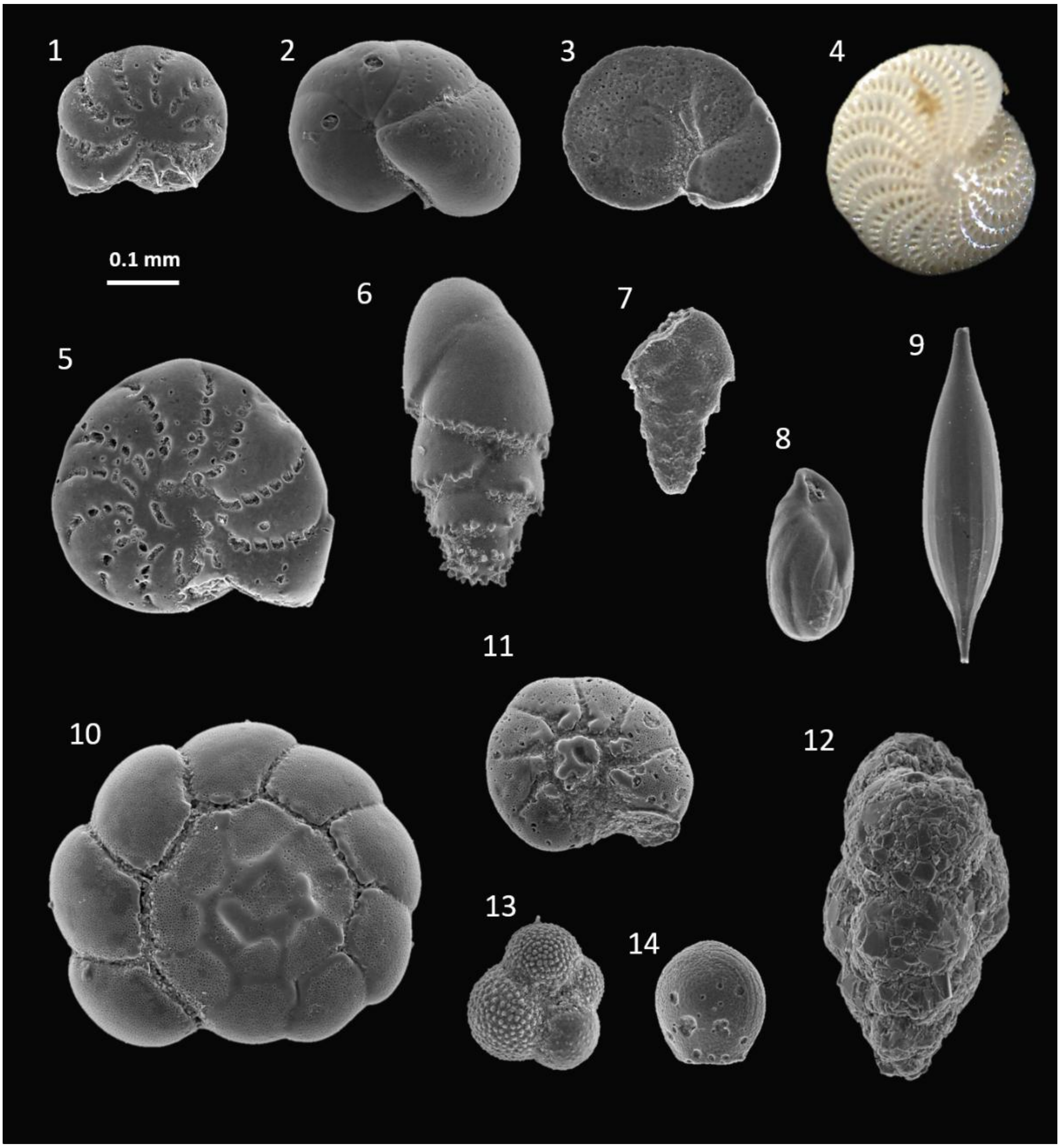

Figure S6. Scanning electron microscopy images and one light photography image of foraminifera of intertidal and shallow marine environments, i.e., potential tsunami sediment sources of Dury Voe (see also Figure S7). 1 – *Haynesina germanica*; 2 – *Cibicides lobatulus* (dorsal); 3 – *C. lobatulus* (ventral); 4 – *Elphidium crispum*; 5 – *Elphidium williamsoni*; 6 – *Bulimina marginata*; 7 – *Bryzalina spathulata*; 8 – *Buliminella elegantissima*; 9 – *Lagena gracilis*; 10 – *Ammonia beccarii* (ventral); 11 – *A. beccarii* (dorsal); 12 – *Egerella scabra*; 13 – *Globigerinoides ruber*; 14 – *Orbulina universa*.

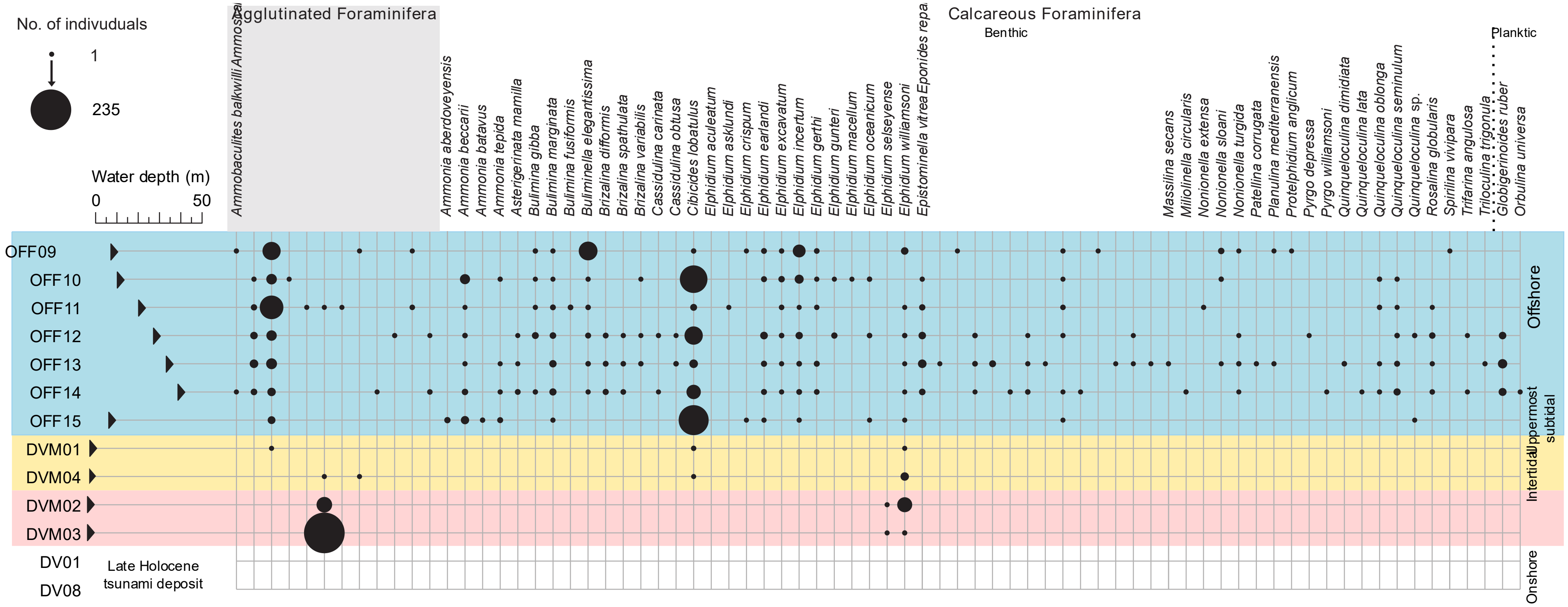

Figure S7. The foraminiferal record of modern intertidal (DVM02, DVM03), subtidal (DVM01, DVM04), and offshore (OFF) sedimentary environments of Dury Voe, representing the most likely source of the late Holocene tsunami deposit. The assemblages are diverse with substantial concentrations in the subtidal, while the onshore tsunami deposits of Dury Voe (DV01, DV08) are void of any tests. For location of sites, see Figure 2A, main text.

Table S7. Heavy mineral distribution of onshore tsunami (DV), modern intertidal and subtidal and modern offshore (OFF) samples from Dury Voe used in this study. Diopside is a calcium-rich clinopyroxene (Mange and Maurer, 1991) but was not sorted into the pyroxene group since it was present in substantial quantities and other identified pyroxenes are only classified as ortho- or clinopyroxenes, not more detailed. For the intertidal and subtidal sample, diopsides were sorted into the pyroxene group (marked with *). The table shows percentages for grains included in the analysis, with quartz, feldspars and contaminations excluded. 2067 total included grains across 8 samples for DV01 and 1496 included grains across 7 samples for DV08.

	DV01 [ø %]	**DV08 [ø %]**	**Intertidal [%]**	**Subtidal [%]**	**OFF09 [%]**	**OFF10 [%]**	**OFF11 [%]**	**OFF12 [%]**	**OFF13 [%]**	**OFF14 [%]**
Epidote group (epidote, zoisite, allanite, mix)	65.41	45.92	50.79	55.57	33.15	40.75	12.27	16.88	20.53	22.59
Amphibole group (hornblende, actinolite, tremolite, unspecified)	17.61	42.78	30.41	24.09	44.99	31.25	59.48	51.10	45.91	36.95
Haematite group (ilmenite, pyrophanite)	4.16	3.01	1.58	-	-	3.00	0.12	-	0.69	1.54
Tourmaline	6.42	2.27	2.32	2.84	1.82	1.50	0.99	1.10	1.27	1.86
Diopside	0.29	0.40	*	*	3.83	3.00	8.80	11.99	10.5	5.81
Mica group (muscovite, biotite, margarite)	2.37	2.94	3.70	1.02	3.09	4.00	0.37	2.05	1.27	1.75
Garnet group (garnet, grossular)	0.48	0.60	0.11	1.02	0.36	2.00	2.60	1.74	3.46	9.87
Pyroxene group (orthopyroxene, clinopyroxene)	0.34	0.60	3.27	2.39	5.28	5.00	8.92	11.67	10.03	7.57
Spinel group (titanomagnetite, magnetite, chromite)	-	-	5.07	-	0.91	7.00	0.61	-	0.12	3.84
Al_2SiO_5 group (andalusite, staurolite)	0.24	0.13	0.11	-	0.55	-	0.87	1.42	0.92	1.32
Titanite	1.01	0.47	1.48	-	0.73	1.75	1.98	1.10	2.65	3.29
Chloritoid	-	-	-	-	0.36	-	0.12	0.16	0.81	1.64
Rutile	0.68	0.47	0.74	0.57	0.18	-	0.50	0.16	-	0.66
Zircon	1.21	0.40	0.32	1.02	0.18	-	0.12	0.16	0.12	0.22
Phosphate group	0.10	-	0.11	-	-	-	-	-	-	0.11
Total included grains	2067	1496	952	875	528	400	807	634	867	912

Table S8. Number of heavy mineral grains analysed in samples from the tsunami deposit and the amount of quartz/feldspar contamination at both onshore locations.

Sample	**Total analysed grains in sample**	**Quartz and feldspar in sample [%]**
DV01/01	353	13.32
DV01/02	332	7.83
DV01/03	301	7.64
DV01/04	189	14.29
DV01/05	376	16.76
DV01/06	217	15.67
DV01/07–08	241	15.36
DV01/09–10	312	30.13
DV08/01	195	6.67
DV08/02	380	7.37
DV08/03	338	10.06
DV08/04	239	15.90
DV08/05	436	20.87
DV08/06	302	80.13
DV08/07–08	91	39.56

Table S9. Stability series of heavy mineral towards weathering as derived from empirical studies and a systematic review (series towards increasing stability).

Series	**Source**	**Studied environment/ evidence**
Apatite < titanite < hornblende < garnet < epidote < zircon	Lång (2000)	Soils developed in tills in southwestern Sweden
Apatite = olivine < amphiboles = pyroxenes < epidotes < garnets < more resistant minerals	Bateman and Catt (1985)	Soils developed in aeolian cover sands in England
Olivine = pyroxene < amphibole < titanite < apatite < epidote = garnet < chloritoid = spinel < staurolite < kyanite < andalusite = sillimanite = tourmaline = rutile = zircon	Morton (1985)	Systematic review of various case studies from sand environments

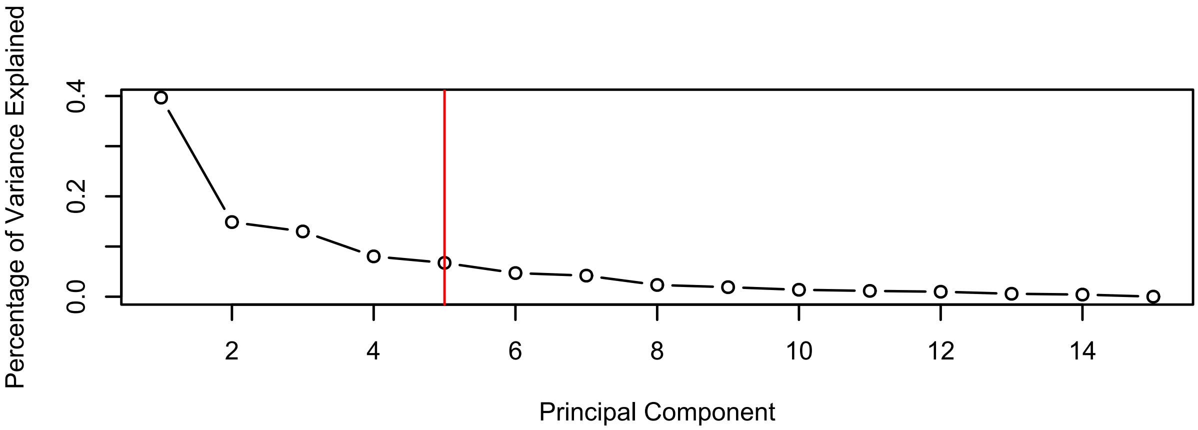

Figure S8. Screeplot of the first 15 principal components from the principal component analysis of the EDX data (see also Figure 8, main text).

Table S10. Hierarchical clustering method selection, internal validation results, and bootstrap robustness assessment (with R packages used).

Test	**Description**	**Result**	**Value(s)**	**R package**
Agglomeration method	Testing the optimal clustering method	Ward’s linkage	0.7921	cluster v2.1.8.1
Internal validation	Determining the optimal number of clusters	2	Connectivity: 5.5103 Dunn Index: 0.4284 Silhouette Width: 0.3802	clValid v0.7
Bootstrapping of dendrogram	Testing robustness of clusters	2 clusters strongly supported	AU values of 0.97 and 0.95	pvclust v2.2-0

References

John W. Anthony, Richard A. Bideaux, Kenneth W. Bladh, and Monte C. Nichols, Eds., Handbook of Mineralogy, Mineralogical Society of America, Chantilly, VA 20151-1110, USA. http://www.handbookofmineralogy.org/ (accessed 17 August 2025).

Bateman RM and Catt JA (1985) Modification of heavy mineral assemblages in English coversands by acid pedochemical weathering. *Catena* 12: 1–21. https://doi.org/10.1016/S0341-8162(85)80001-1

Blaauw M, Aquino-López M, Christen JA (2024) Modelling chronologically ordered radiocarbon dates in R. *Radiocarbon*. https://doi.org/10.1017/RDC.2024.56

Bondevik S, Mangerud J, Dawson S, Dawson A and Lohne Ø (2005) Evidence for three North Sea tsunamis at the Shetland Islands between 8000 and 1500 years ago. *Quaternary Science Reviews* 24: 1757–1775. https://doi.org/10.1016/j.quascirev.2004.10.018

Hess K, Engel M and Koutsodendris A (2023) Sedimentological storm and tsunami record of Loch Flugarth, Shetland Islands (UK). heiDATA. https://doi.org/10.11588/data/QJEZHT

Hess K, Engel M, Patel T, Vakhrameeva P, Koutsodendris A, Klemt E, Hansteen TH, Kempf P, Dawson S, Schön I and Heyvaert VMA (2024) A 1500-years record of North Atlantic storm flooding from lacustrine sediments, Shetland Islands (UK). Journal of Quaternary Science 39: 37–53. https://doi.org/10.1002/jqs.3568

Klein C and Hurlbut CS (1985) *Manual of mineralogy* (20th ed). New York: Wiley.

Lång L-O (2000) Heavy mineral weathering under acidic soil conditions. *Applied Geochemistry* 15: 415–423. https://doi.org/10.1016/S0883-2927(99)00064-5

Leveneur J, Trompetter WJ, Chong SV, Rumsey B, Jovic V, Kim S, McCurdy M, Anquillare E, Smith KE, Long N, Kennedy J, Covic G and Boys J (2021) Ironsand (titanomagnetite-titanohematite): Chemistry, magnetic properties and direct applications for wireless power transfer. *Materials* 14: 5455. https://doi.org/10.3390/ma14185455

Mange MA and Maurer HF (1991) *Schwerminerale in Farbe*. Stuttgart: Enke.

Morton AC (1985). Heavy minerals in provenance studies. In: Zuffa GG (ed) *Provenance of Arenites*. Dordrecht: Springer, pp.249–277. https://doi.org/10.1007/978-94-017-2809-6_12

Reimer PJ, Austin WEN, Bard E, Bayliss A, Blackwell PG, Bronk Ramsey C, Butzin M, Cheng H, Edwards RL, Friedrich M, Grootes PM, Guilderson TP, Hajdas I, Heaton TJ, Hogg AG, Hughen KA, Kromer B, Manning SW, Muscheler R, Palmer JG, Pearson C, van der Plicht J, Reimer RW, Richards DA, Scott EM, Southon JR, Turney CSM, Wacker L, Adolphi F, Büntgen U, Capano M, Fahrni SM, Fogtmann-Schulz A, Friedrich R, Köhler P, Kudsk S, Miyake F, Olsen J, Reinig F, Sakamoto M, Sookdeo A, Talamo S (2020) The IntCal20 Northern Hemisphere radiocarbon age calibration curve (0–55 cal kBP). *Radiocarbon* 62, 725–757. https://doi.org/10.1017/RDC.2020.41